KIMBERLITIC OLIVINE

by

RICHARD CURTIS BRETT

B.Sc. Honours, Carleton University, 2005

A THESIS SUBMITTED IN PARTIAL FULFILMENT OF THE REQUIREMENTS FOR THE DEGREE OF

MASTER OF SCIENCE

in

The Faculty of Graduate Studies

(Geological Science, Earth and Ocean Sciences)

THE UNIVERSITY OF BRITISH COLUMBIA
(Vancouver)

February, 2009

ABSTRACT

Kimberlite hosts two populations of olivine that are distinguished on the basis of grain size and morphology; the populations are commonly described genetically as xenocrysts and phenocrysts. Recent studies of zoning patterns in kimberlitic olivine phenocrysts have cast doubt on the actual origins of the smaller olivine crystals. Here, we elucidate the nature and origins of the textural and chemical zonation that characterize *both* populations of olivine. Specifically, we show that both olivine-I and olivine-II feature chemically distinct overgrowths resulting from magmatic crystallization on pre-existing olivine xenocrysts. These results suggest that the total volume of olivine crystallized during transport is substantially lower (≤5%) than commonly assumed (e.g. ~25%), and that crystallization is dominantly heterogeneous. This reduces estimates of the Mg# in primitive kimberlite melt to more closely reconcile with measured phenocryst compositions.

Several additional textures are observed in olivine, and include: sealed cracks, healed cracks, phases trapping in cracks, rounded grains, overgrowths and phase trapping in overgrowths. These features record processes that operate in kimberlite during ascent, and from these features we create a summary model for kimberlite ascent:

- Olivine is incorporated into kimberlitic melts at great depths as peridotitic mantle xenoliths.
- Shortly after the incorporation of these xenocrysts the tensile strength of the crystals within xenoliths is reached at a minimum of 20 km from its source. Disaggregation of mantle xenoliths producing xenocrysts is facilitated by expansion of the minerals within the xenoliths.

- The void space produced by the failure of the crystals is filled with melt and crystals consisting of primary carbonate (high-Sr), chromite and spinel crystals. The carbonate later crystallizes to produce sealed fractures.
- Subsequent decompression causes cracks that are smaller than the sealed cracks and are preserved as healed cracks that crosscut sealed cracks.
- Mechanical rounding of the xenocrysts post-dates, and/or occurs contemporaneously with decompression events that cause cracking.
- Saturation of olivine produces rounded overgrowths on large xenocrysts, euhedral overgrowths on smaller xenocrysts, and a volumetrically minor population of olivine phenocrysts. Olivine growth traps fluid, solid and melt inclusions.

Calculations based on these relationships suggest that the melt saturates with olivine at a maximum depth of 20 km and a minimum depth of 7 km.

TABLE OF CONTENTS

LIST OF TABLES

LIST OF FIGURES

ACKNOWLEDGMENTS

This research was funded by an NSERC Collaborative Research and Development Grant (Kimberlite eruption dynamics: Implications for diamond distribution in the Diavik kimberlite) held by Kelly Russell and sponsored by Diavik Diamond Mines, Inc. (DDMI). I acknowledge many beneficial conversations with Terence Gordon and Barbara Scott-Smith. I also thank Professor Mati Rausdupp for guidance in obtaining and processing electron microprobe analyses and Jenny Lai for her help.

Foremost, thank you my supervisor Kelly. I am astounded by Kelly's infinite passion and enthusiasm. This created an exciting and enjoyable environment to work in. Thank you.

Thank you to the VPL lab for their comradeship and help with this thesis. I especially thank Steven Moss for countless discussions and who contributed ideas, helped with sample collection, and help with this thesis, it surely made it better. Genevieve, Jackie, Nils, R.E., Graham and all graduate students who I shared many wonderful moments with, thank you. Thanks to all my friends that I have met in Vancouver and to all the people back east.

Thank you to my love, Tiffany, for her support and help throughout this thesis, my parents, Dave and Jill, and family for all the love and support.

Lastly thanks to my brother Dan, who taught me that no matter how hard life gets, keep your head high and to charge straight ahead. I will always strive to do this, but will never be able to match your strength.

CO-AUTHORSHIP STATEMENT

This thesis comprises two complementary manuscripts prepared for publication in peer-reviewed international scientific journals. Chapter II has been accepted subject to revision (LITHOS2161; November 2008), in a special volume of Lithos (9th international kimberlite conference, Eds. Koole), under the title "The origin of olivine in kimberlite: phenocryst or impostor". I am senior author, and my co-authors are Kelly Russell and Steven Moss. Chapter II presents a textural and geochemical study of olivine in kimberlite, and subsequently explores the chemical implications. Samples used for this study were logged and collected at Diavik with the help of Steve Moss. Steve Moss also provided the measured olivine crystal distributions used as input for modeling crystal growth.

Chapter III is also intended for publication in an international journal under the title "Kimberlite ascent: Insights from olivine". Chapter III presents additional textural observations and semi-quantitative calculations of kimberlitic olivine with the intent to constrain processes operative in the ascent of kimberlite. Crystal modeling codes were written by myself, and Kelly Russell assisted with problems associated with geological relevance, and modeling methods.

1. Introduction

Kimberlitic melts derive from depths > 200 km and transport samples of Earth's mantle to the surface. Deep-seated volcanic activity is the only way to directly study natural mantle samples, and is the only process that allows study and extraction of valuable high-pressure minerals. Olivine is the most abundant phase in kimberlite deposits, and an understanding of olivine is paramount to understanding the petrogenesis of kimberlite.

There are two types of olivine in kimberlite, and they have different origins: xenocrysts and phenocrysts. Xenocrysts, are derived from disaggregated mantle peridotite and/or dunite, and tell us about, i) the composition of the mantle (e.g. Griffin, 2003) and ii) stress-fields in the mantle (e.g. Kennedy et al., 2002). Olivine derived from crystallization of the melt has consequences for kimberlite melt composition (e.g. Price et al., 2001) and has been linked to the dissolution of orthopyroxene in kimberlite melts (e.g. Mitchell, 2008). Olivine hosts a variety of primary inclusions, including: i) mineral inclusions, which can be used to constrain olivine saturation temperatures (Fedortchouk & Canil, 2004), ii) melt inclusions (Roedder, 1965; Sobolev et al., 1989), which can yield information on melt compositions, liquidus temperatures and olivine growth, and iii) fluid inclusions that record information on the volatile content of the melt, and the conditions (P, T) for vesiculation. All of these insights are important for reconstructing the petrogenesis of kimberlite. Interpretation of data deriving from these inclusions is dependent on the origin of the olivine.

Debate on the origin of olivine has lasted more than a century; the early works of Wagner (1914), Williams (1932) and Dawson (1962) recognized and described the two

texturally distinct types of olivine in kimberlite, but interpreted them as different generations of phenocrystic crystallization. Both types were, thus, viewed as crystals cogenate to the kimberlite melt. Verhoogen (1938) and Davidson (1943) recognized the foreign nature of peridotite 'inclusions' and 'nodules' of ilmenite, garnet and pyroxene in kimberlite and postulated that they derived from the Earth's peridotitic mantle or from the metamorphic basement. Subsequently, the term 'macrocryst' is used to describe grains between 0.2 and 5 mm in diameter (Dawson 1980, Clement 1982), and the term 'megacryst' reserved for larger grains as a non-genetic descriptive term. The compositions of garnet, olivine and diopside in mantle peridotite were then compared against the macrocrysts in kimberlite and found to be similar in composition (Boyd 1967, Reid & Hanor 1970), For this reason the macrocrystic minerals in kimberlite were interpreted to resulted from broken up xenoliths of garnet lherzolites and eclogites. The origin of the euhedral 'phenocrystic' olivine is ascribed to homogeneous crystallization and is identified on the basis of crystal morphology and crystal size alone (Mitchell, 1995). There are a few geochemical studies designed to elucidate the differences between xenocrystic and phenocrystic olivine in kimberlite. One such example was the work of Clement (1982), documented the major element compositional differences in many of the African kimberlites. Specifically, his work showed, that, on average, euhedral olivine had lower forsterite contents than typical of the macrocrystic olivine grains (Fo_{89} vs. Fo_{93}). Several later studies have substantiated these compositional differences between xenocrystic and euhedral olivine (Skinner 1986; Boyd and Clement, 1977; Dawson, 1994).

More recent studies concerning the origin of olivine in kimberlite include the efforts of Hearn (2004), Fedortchouk & Canil (2004) and Kamenetsky et al. (2007). Hearn (2004) analysed compositions of xenocrystic olivine that featured chemically distinct euhedral overgrowths, and suggested their origin to be magmatic. Kamenetsky et al. (2008) presented results on zoning patterns found in olivines classified as phenocrysts. Many of the smaller olivine grains featured sub-rounded to rounded cores and chemically distinct euhedral rims. Moreover, the cores of these crystals have affinities to xenocrystic olivine compositions, and even contain calcic-pyroxene inclusions of mantle origin in these cores. In light of these recent works, it is evident that olivine within kimberlite may not represent a simple bimodal population of phenocrysts and xenocrysts.

Here, the textural features found in kimberlitic olivine are described. These features and their relative timing are then explored in terms of their implications for the ascent of kimberlite. We use samples from the Diavik Diamond Mine because these deposits are relatively young and preservation of the deposits is excellent. The Diavik Diamond Mine property is on East Island, located within the Lac de Gras area of the Slave Craton approximately 300 km North of Yellowknife in the central Northwest Territories, Canada (Fig. 1.1). We sampled from four kimberlite pipes, (A154N, A154S, A418, A21), which are Eocene in age (55-56 Ma; Graham et al., 1998). These pipes intrude Archean granitoids and metaturbidites and are overlain by surficial deposits resulting from Late Pleistocene glaciations that peaked 20 ka before present (Briner et al., 2003). The pipes form near vertical cones that have been identified to penetrate basement rocks more than 600 m below the present day surface. The surface expression of each pipe ranges 100-150 m in diameter.

Although ideas explored in this thesis derive from a few samples collected from 3 pipes within a single kimberlite field, we suggest that extrapolation of these ideas to kimberlite deposits worldwide is valid. Globally, the mineralogy of kimberlite is strikingly consistent in time and space (Field and Scott Smith, 1999), and the Diavik kimberlite is representative of kimberlite mineralogy. Furthermore, several other published studies on kimberlitic olivine corroborate many of our textural and chemical observations (e.g. Homestead kimberlite in U.S.A. (Eocene), Carter Hearn (2004); Lac de Gras cluster in Canada (Late Cretaceous to Eocene), Fedortchouk & Canil (2004); and the Udachnaya-East kimberlite in Russia (Carboniferous), Kamenetsky et al., (2007). All of these studies report chemical zoning of Ni, Fe, and Mg in olivine, and recognize mineral inclusions in the overgrowths.

Despite these works, there are many studies on kimberlitic olivine that do not report zoning in olivine. There are two possibilities for this discrepancy: 1) No zoning in these studies exists, or 2) zoned olivine exists, but was not recognized. The ability to observe zoning produced by overgrowths is highly dependent on the preservation of the mineral. For example, olivine in kimberlite is commonly pervasively serpentinized and/or replaced by carbonate. This alteration masks and erases overgrowths, or zoned features, rendering identification of these features impossible. Even very minor alteration around the edges of crystals can make identification and recognition of any chemical zonation and overgrowth very difficult. On this basis, we submit that features described in olivine within the Diavik kimberlites are representative other kimberlites worldwide. The processes that operate on kimberlite from source (mantle) to eruption must be consistent between kimberlite localities worldwide in order to produce the consistency in

mineralogy, texture, and deposit type observed at other localities. The attendance of olivine for arguably the entire ascent of kimberlite means that any process that happened during ascent has the potential to be recorded in olivine. Many of the Diavik samples are pristine and are not altered making them exceptional candidates for compositional analysis.

The first question asked is: what is the significance of the petrographic and chemical zoning observed in kimberlitic olivine? This question is approached with a thorough textural description and geochemical study of zoned olivine in the Diavik deposits, and is presented in chapter 2. The composition and quantity of olivine that crystallized from the kimberlite melt has implications on the composition of the melt, and has been linked with the dissolution of orthopyroxene, a peridotitic and eclogitic mineral rarely observed in kimberlite deposits. It is important that when using olivine, or features associated with olivine (i.e. fluid inclusions, chemical zoning) to deduce properties of the system (e.g. T, P, X) that the origin of the olivine is known with confidence.

In addition to the textural and chemical zoning found in kimberlitic olivine, there are several additional textural features related to volcanic processes including: primary inclusions, pseudo-secondary inclusions, rounded grains, decompression cracks, healed fractures and sealed fractures. Crosscutting relationships of many of these textures are also observed. The second question that we asked is: can we deduce processes that caused these textural features in olivine? Can we use the physical properties of olivine to constrain the depth at which these processes were operative? Solutions to these questions force constraints on kimberlite ascent from source to surface. A description of each textural feature and a discussion of their formation are presented in chapter 3.

Figure 1.1. Location of Diavik and kimberlite pipes near East Island.
From Moss et al. 2008

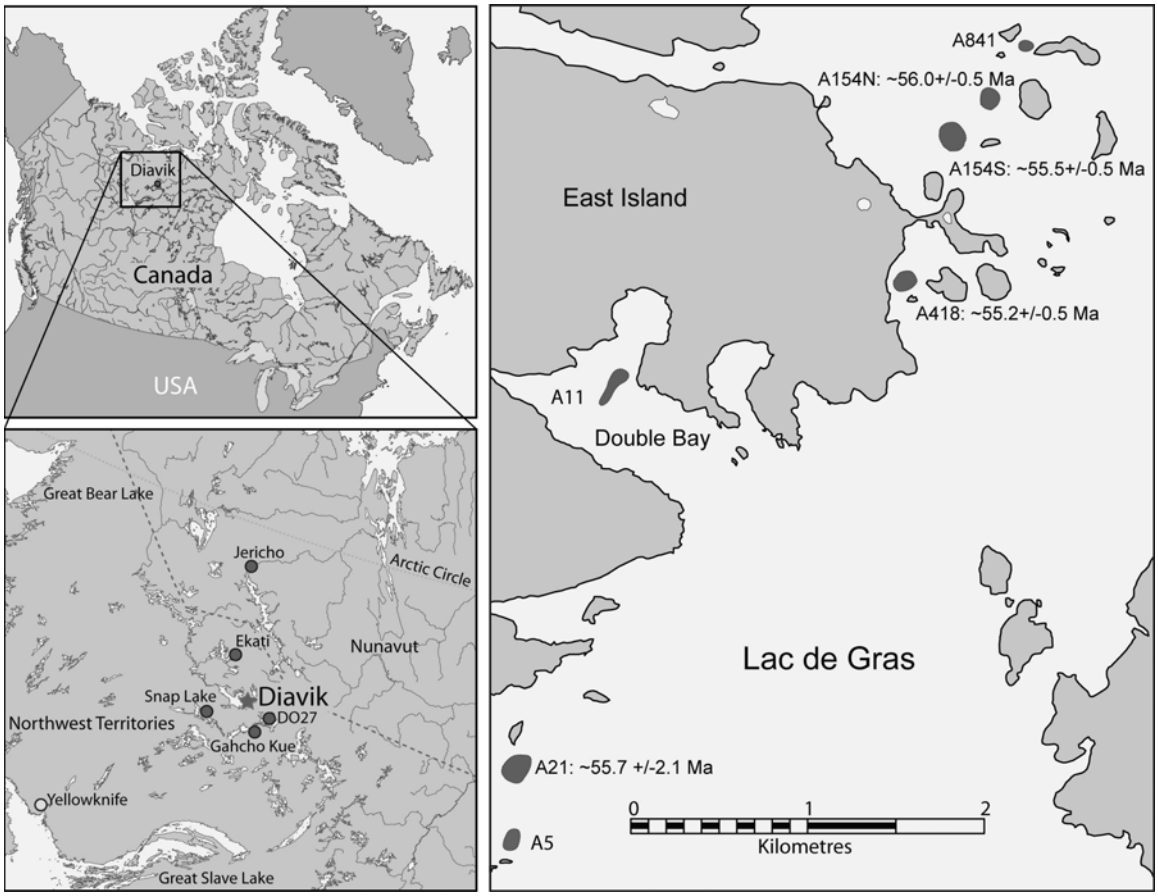

1.2 List of references

Boyd, F.R., 1967. Electron microprobe analyses of diopsidic pyroxenes from kimberlites. Annual Report Carnegie Institute of Washington, 65, 252-260.

Briner, J. P., Miller, G.H., Davis, P.T., Bierman, P.R., Caffee, M., 2003. Last glacial maximum ice sheet dynamics in Artic Canada inferred from young erratics perched on ancient tors. Quaternary Science Reviews, 22, 437-444.

Clement, C.R., 1982. A comparative geologic study of some major kimberlite pipes in the Northern Cape and Orange Free State. Ph.D. Thesis. Department of Geology, University of Cape Town.

Davidson, C.F., 1943. The Archean rocks of the Rodil district, South Harris, Outer Hebrides. Transactions of the Royal Society of Edinburgh, 61, 71-112.

Dawson, J.B., 1962. Basutoland kimberlites. Geological Society of America Bulletin, 73, 545-560.

Dawson, J.B., 1971. Advances in kimberlite geology. Earth Science Reviews, 7 , 187-214.

Dawson, J.B., 1980. Kimberlites and their xenoliths. Springer.

Dawson, J.B., 1994. Quaternary kimberlitic volcanism on the Tanzania Craton. Contributions to Mineralogy and Petrology 116, 473–485.

Fedortchouk, Y., Canil, D., 2004. Intensive variables in kimberlite magmas, Lac de Gras, Canada and implications for diamond survival. Journal of Petrology, 45 1725-1745.

Field M. and Scott Smith B.H., 1999. Contrasting Geology and Near-Surface Emplacement of Kimberlite Pipes in Southern Africa and Canada. Proceedings of the Seventh International Kimberlite Conference, Vol. 1, p. 214-237.

Graham, I., Burgess, J.L., Bryan, D., Ravenscroft, P.J., Thomas, E., Doyle, B.J., Hopkins, R., Armstrong, K.A., 1998. Exploration history and geology of the Diavik kimberlites, Lac de Gras, Northwest Territories, Canada. In: Gurney, J.J., Gurney, J.L., Pascoe, M.D., Richardson, S.H. (Eds.), Proceedings of the VIIth International Kimberlite Conference. Red Roof Design, Cape Town, South Africa, pp. 262–279. Griffin, 2003

Hearn, B.C. Jr., 2004. The Homestead kimberlite, central Montana, USA: mineralogy, xenocrysts, and upper-mantle xenoliths. Lithos, 77, 473-491.

Kamenetsky, V.S., Kamenetsky, M.B., Sobolev, A.V., Golovin A.V., Demouchy, S., Faure, K., Sharygin V.V., Kuzmin, D.V., 2008. Olivine in the Udachnaya-East Kimberlite (Yakutia, Russia): Types, compositions and origins. Journal of Petrology, 49, 823-839.

Kennedy, L.A., Russell, J.K., Kopylova, M.G., 2002. Mantle shear zones revisited: The connection between the cratons and mantle dynamics. Geology, 30, 419-422.

Mitchell, R.H., 1995. Kimberlites, Orangeites, and Related Rocks. Plenum Press, New York.

Mitchell, R.H., 2008. Petrology of hypabyssal kimberlites: Relevance to primary magma compositions. Journal of Volcanology and Geothermal Research, 174, 1-8.

Moss, S., Russell, J.K., Andrews, G.D.M., 2008. Progressive infilling of a kimberlite pipe at Diavik, Northwest Territories, Canada: Insights from volcanic facies architecture, textures, and granulometery. Journal of Volcanology and Geothermal Research, 174, 103-116.

Price, S.E., Russell, J.K., Kopylova, M.G., 2000. Primitive magma from the Jericho pipe, N.W.T., Canada: Constraints on primary kimberlite melt chemistry (41) 6, 789-808.

Reid, A.M., Hanor, J.S., 1970. Pyrope in kimberlite. American Mineralogist, 55, 1374-1379.

Roedder, E. 1984. Fluid Inclusions; Reviews in Mineralogy In Mineralogical Society of America.

Roedder, E., 1965. Liquid CO_2 inclusions in olivine-bearing nodules and phe ocrysts from basalts. American Mineralogists, 50, 1746-1782.

Skinner, E.M.W., 1986. Contrasting Group I and Group II kimberlite petrology: towards a genetic model for kimberlites. Proceedings of the fourth international kimberlite conference, Volume 1, 528-544.

Sobolev, A.V., Sobolev, N.V., Smith, C.B., Dubessy, J., 1989. Fluid and melt compositions in lamproites and kimberlites based on the study of inclusions in

olivine. GAS Special Publication No. 14: Kimberlites and related rocks, their composition, occurrence origin and emplacement, volume 1.

Wagner, P.A., 1914. The Diamond Fields of Southern Africa. The Transvaal Leader, Johannesburg.

Williams, A.F., 1932. The Genesis of the Diamond. Ernest Benn, London.

Verhoogen, J., 1938. Les pipes de kimberlite du Katanga: Commun. Spéc. Katunga Ann. Services Mines, 9 1-15.

2. Origin of Olivine in Kimberlite: Phenocryst or Impostor?[1]

2.1 Introduction

Olivine is the dominant phase in all kimberlite bodies and a petrogenetic model for kimberlite must, therefore, include a complete explanation for the origins of olivine. The olivine hosted by kimberlite forms two populations that are distinguished on the basis of grain size and morphology (Clement et al., 1977; Skinner & Clement, 1979). The volumetrically most important population comprises grains of olivine that are medium to coarse-grained, rounded to sub-rounded, and are referred to as macrocrysts (Clement, 1982). The second population features medium to fine-grained (< 0.5 mm), euhedral to subhedral olivine grains and are commonly designated as phenocrysts. For over 30 years the two populations of olivine found in kimberlite have been ascribed different origins as encapsulated by their labels; the macrocrysts are xenocrystic whilst the phenocrysts are assumed to have crystallized from the kimberlite melt.

Our study of kimberlite from the Diavik Diamond Mine, N.W.T, Canada shows the olivine within these deposits to comprise rounded to sub-rounded cores featuring distinct overgrowths of later crystallized olivine. In all samples we observe overgrowths on both 'macrocrystic' and 'phenocrystic' olivine crystals. The goal of this manuscript is to elucidate the origins of these overgrowths, and to explore the implications of these origins.

Here, we present textural and geochemical data on olivine grains derived from 7 samples of kimberlite. Our sample suite includes coherent intrusive kimberlite and

[1] A version of this chapter has been accepted for publication pending revision. Brett, R.C., Russell, J.K., Moss, S. (2009) Origin of olivine in kimberlite: Phenocryst or impostor? Lithos, submitted September 20, 2008.

pyroclasts from volcaniclastic kimberlite deposits. These data show that the cores of all olivine grains have overlapping chemical compositions and that the overgrowths are compositionally distinct from their respective cores. We suggest that virtually all olivine within kimberlite has a xenocrystic origin and derives from disaggregated mantle peridotite. This would substantially reduce the amount of olivine crystallization during transport relative to previous estimates (up to 25%; Clement, 1982; Scott Smith, 1996; Harris et al., 2004; Mitchell, 2008). The reduced extent of olivine crystallization has important implications on: i) estimates of primitive kimberlite melt compositions (e.g. Price et al., 2000) and on, ii) the extent of orthopyroxene dissolution and melt modification attending kimberlite ascent (e.g. Mitchell, 1986).

2.2 Kimberlite sample suite

The Diavik Diamond Mine property is located within the Lac de Gras area of the Slave Craton approximately 300km North of Yellowknife in the Northwest Territories, Canada. Four kimberlite pipes are currently in the Diavik mine plan, (A154N, A154S, A418, A21) and are Eocene in age (55-56 Ma; Graham et al., 1998). Crosscutting relationships between the 4 pipes are not observed, and they must be considered as coeval given the uncertainties on the radioactive age dates (Rb-Sr, mica; Graham et al., 1998).

Our intent is to document the textural and chemical attributes of olivine within, both, coherent intrusive kimberlite dykes and volcaniclastic kimberlite units. We selected five samples of coherent kimberlite from dykes associated with three of the Diavik pipes (Table 2.1). The samples were selected to minimize the effects of secondary alteration. In these samples olivine is not serpentinized even along grain margins or internal factures. Whole rock chemical compositions for the samples of coherent kimberlite are given in

Table A1. In terms of the major constituents (SiO_2, MgO, CaO and FeO (T)), the Diavik chemical compositions are similar to other 'fresh' kimberlite analysed (Price et al., 2000; Dawson, 1994, Caro et al., 1994). Two samples were also collected from separate volcaniclastic kimberlite deposits (Table 2.1) described previously by Moss et al., (2008).

Table 2.1. List of samples and descriptions of source, deposit type and olivine content.

Label[(1)]	Kimberlite pipe	Unit	Facies	Vol. % olivine	Reference
1	A154 north	Late dyke	Coherent	41	Moss et al., 2008b
2	A154 north	Late dyke	Coherent	40	-
3	A154 north	Late dyke	Coherent	50	-
4	A154 south	Late dyke	Coherent	45	-
5	A21	Late dyke	Coherent	40	-
6	A154 north	MVK	Volcaniclastic	70	Moss et al., 2008a
7	A154 north	GK	Volcaniclastic	53	Moss et al., 2008a

[1]1:A154N_08_pet02; 2:A154N_10_12; 3:A154N09_07; 4:A154_35_03; 5:A21_GT03_01; 6:GTH_75_17_01; 7:A154N_340_GK_B02; MVK = Massive volcaniclastic kimberlite; GK = Graded kimberlite

2.3 Petrography

The kimberlite samples contain 40 - 50 volume % olivine (Table 2.1), and on the basis of grain size and morphology, the olivine constitutes two distinct populations: a) medium to coarse-grained (< 2 cm), rounded to sub-rounded crystals (olivine-I, Fig. 2.1a), and b) fine-grained (< 1 mm), euhedral to subhedral crystals (olivine-II, Fig. 2.1b). The samples also contain macrocrystic garnet (< 2%), clinopyroxene (< 2%) and orthopyroxene (< 1%). Groundmass minerals identified petrographically, in order of decreasing abundance, include: olivine, oxides, monticellite, apatite and perovskite. The groundmass mineralogy includes equant oxides consisting of chromite spinels with overgrowths of ulvöspinel – spinel that are, in some samples, rimmed with dark-brown, transparent serpentine. These minerals are commonly euhedral and enclosed by a carbonate-serpentine mesostasis. Occasionally, carbonate is found to enclose groundmass minerals and xenocrysts in poikioblasts. In most samples, monticellite is present only

within carbonate-rich portions of the matrix whilst olivine, oxides and apatite occur in both carbonate and serpentine domains.

Pyroclastic deposits comprise mainly individual, broken (angular) olivine crystals that have essentially no selvages of kimberlite magma (i.e., free olivine grains), small (<1 cm in diameter) juvenile pyroclasts of kimberlite, and accessory country rock fragments cemented together by a matrix of yellow-brown coloured serpentine. Olivine is more abundant in the pyroclastic kimberlite deposits than in samples of coherent kimberlite (Table 2.1). Olivine within juvenile pyroclasts of kimberlite is fresh and shows little serpentinization. Juvenile pyroclasts also contain euhedral, square-shaped oxides and feature a matrix of serpentine and minor carbonate.

Rounded to sub-rounded peridotite and dunite microxenoliths are common as accidental lithics in samples of kimberlite from Diavik. Olivine within mantle xenoliths occurs as 0.01 mm to 1 mm, serrated to euhedral crystals. These mantle-derived xenoliths commonly contain neoblasts of olivine grains that result from recrystallization of earlier deformed olivine during kimberlite transport (Arndt et al., 2006) or from recrystallization in the mantle before being entrained by kimberlite (Ross, 1983; Kennedy et al., 2002). The neoblastic olivine occurs as unstrained, single tabular crystals up to 1 mm in length and may be completely enclosed by larger, strained olivine xenocrysts (Fig. 2.1e). Some large strained xenocrysts (< 1cm) of olivine feature clusters of small (< 0.1 mm), euhedral to subhedral neoblasts of olivine (Fig. 2.1f) that are unstrained, lack mineral or fluid inclusions, and occasionally show weak crystallographic alignment. The neoblastic olivine grains have grain sizes and crystal habits equivalent to those described for the classical kimberlitic olivine phenocrysts.

Figure 2.1. Photomicrographs of olivine from Diavik kimberlite deposits

Photomicrographs of olivine from Diavik kimberlite deposits, showing: a) xenocrystic olivine (olivine-I) comprising anhedral, rounded to sub angular, inequigranular crystals, b) "*phenocrystic*" olivine (olivine-II) identified as smaller (< 1mm), euhedral to subhedral crystals, c) overgrowth on olivine macrocryst (olivine-I) defined by increase in concentration of inclusions, d) enlarged view of olivine-II crystal showing euhedral overgrowth on rounded core, e) mantle xenolith containing mm-scale band of polycrystalline recrystallized olivine grains, f) enlarged view of polycrystalline recrystallized olivine showing characteristic grain size (< 1mm) and subhedral to euhedral habit.

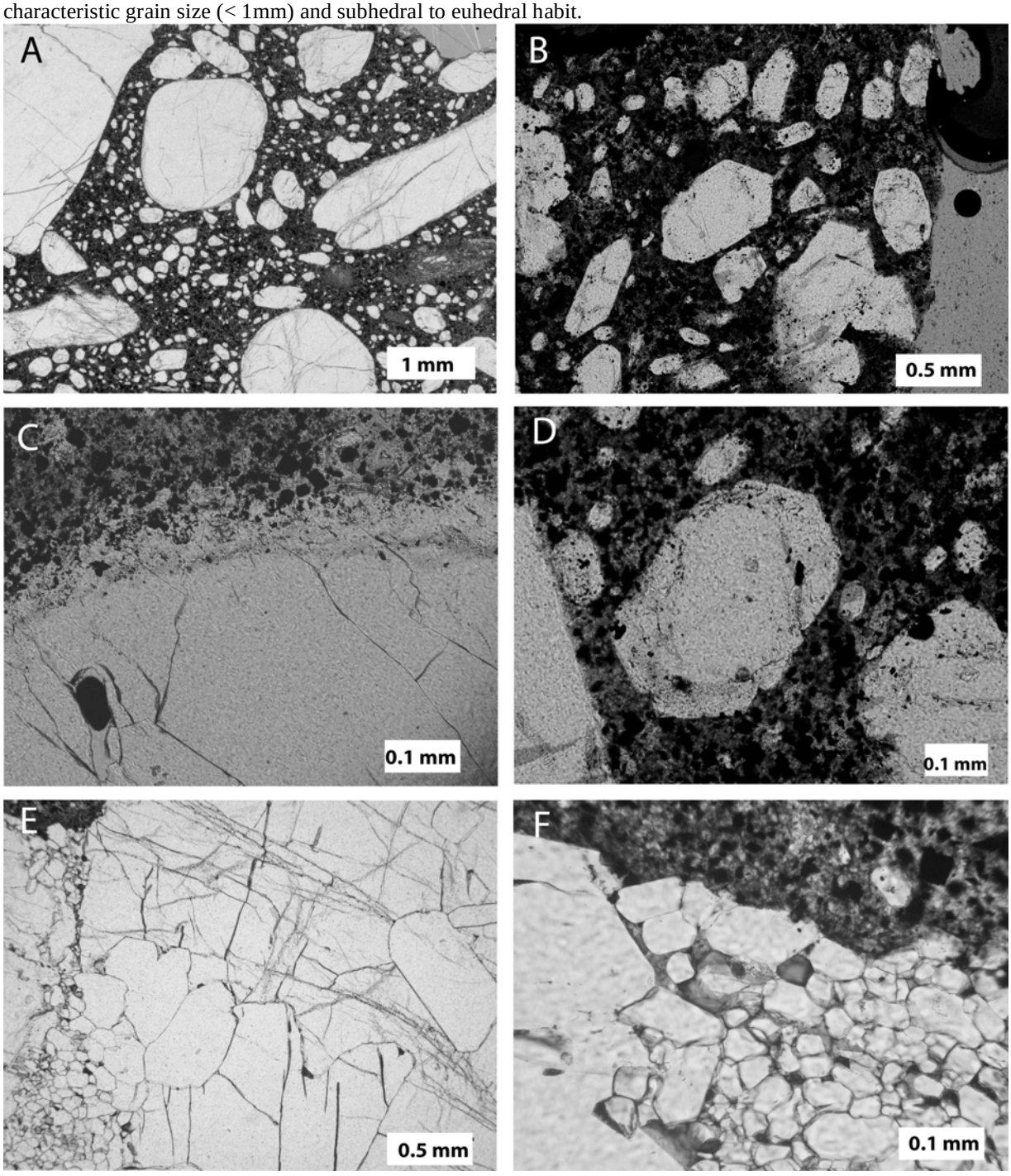

2.4 Petrographic zonation in olivine

Olivine (xenocrysts and phenocrysts) in kimberlite can show complex zoning patterns. Recently, Kamenetsky et al. (2008) presented results on zoning patterns found in olivines classified as phenocrysts. The chemical characterization of these olivine grains showed that the cores to these grains have chemical affinities to the xenocrystic olivine (i.e. macrocrysts). On that basis, Kamenetsky et al. (2008) proposed the terms olivine-I and olivine-II to avoid the genetic connotations of xenocrysts and phenocrysts, respectively. For the purposes of this research we have adopted their terminology. Within our suite of kimberlite samples, olivine-I (Fig. 2.1c) and olivine-II (Fig. 2.1d) have petrographically visible overgrowths of olivine that are partly defined by the presence of mineral, fluid and melt inclusions (Fig. 2.2). The original cores, for both types of olivine grains, are inclusion free and are commonly rounded to sub-rounded in shape. Overgrowths do not change the overall shapes of olivine-I grains because the rims are thin (< 0.12 mm) relative to the diameter of the original grain (Fig. 2.1c; Fig. 2.3b). In contrast, the shapes of the olivine-II grain are strongly modified by the overgrowths; the rims are commonly sufficiently thick, relative to the original grain diameter, to create euhedral morphologies (Fig. 2.1d; Fig. 2.3a - c).

As stated above, the interface of the core-overgrowth boundary is commonly marked by the presence of numerous, small (< 5 μm) spherical fluid inclusions (Fig. 2.2). The fluid inclusions in Fig. 1c and 1d are seen as the dark band at the core-overgrowth boundary. The magnified view in Fig. 2.2 shows the diversity of daughter products present in the olivine overgrowths, whilst the inset (Fig. 2.2) shows ‘bubble’ planes marking the core-overgrowth boundary. Mineral inclusions are often small at this

boundary (< 1μm) but increase in size towards the edge of the crystal. Mineral inclusions are identified petrographically as opaque oxides, rutile and perovskite. Opaque minerals were confirmed with scanning electron microscopy (SEM) as predominantly magnesium-rich chromites and ulvöspinel – spinel solid solution mineral inclusions. Larger (<60 μm), irregular-shaped melt inclusions are trapped by overgrowths, and are dominantly composed of carbonate (Fig. 2.2).

False coloured, back-scattered micrographs of olivine show the nature of compositional zoning in several samples (Fig. 2.3), where darker shades of red correspond to more forsterite rich regions. Olivine grains can show normal (Fig. 2.3a), reverse (Fig. 2.3c) or, in many cases, show no zoning (i.e., homogeneous; Fig. 2.3c). The compositional zoning seen in Figure 2.3 corresponds to the overgrowths seen petrographically (Fig. 2.1c - d). The overgrowths also show a zoning that commonly terminates as a thin, (< 5 micron) dark coloured rim (Fig. 2.3c). These outermost rinds of olivine have extremely high forsterite content (Fo_{96-98}) and contain up to 2 wt.% CaO, and have been described in other kimberlite deposits (Kamenetsky et al., 2008; Arndt et al., 2006; Scott Smith, pers. com.).

Figure 2.2. Inclusions within olivine
Photomicrograph of olivine shown in Figure 2.1d. Increased magnification shows the diversity of inclusions in olivine overgrowths including: opaque minerals, apatite, perovskite, and fluid inclusions. The inset shows planes (p) of fluid inclusions marking the core-overgrowth boundary.

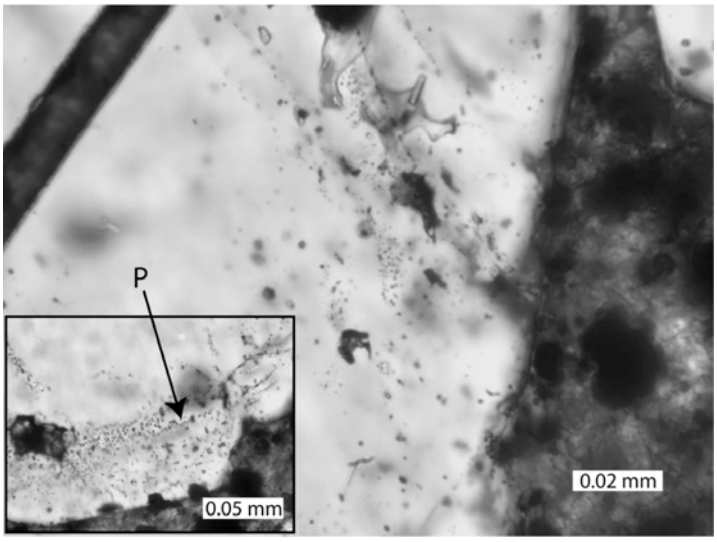

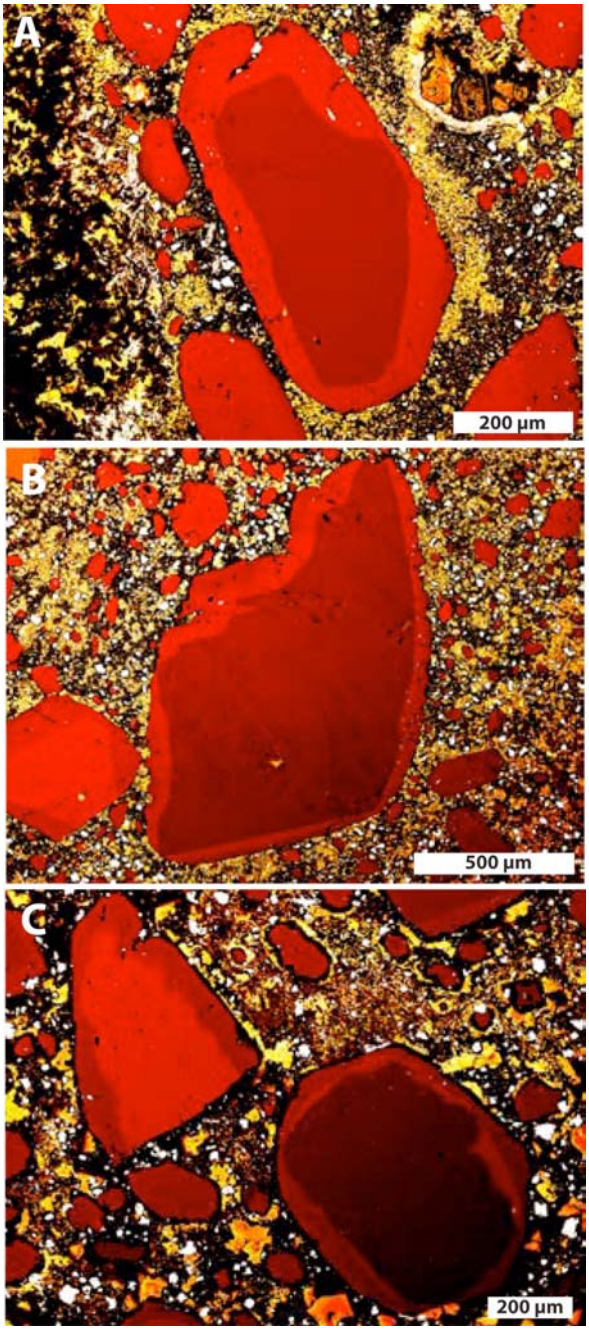

Figure 2.3. False coloured back scattered micrographs of olivine
False coloured back scattered micrographs of olivine crystals (red colours) showing major element zoning and overgrowth morphology in: a) normally zoned olivine-II crystal where overgrowth changes the original shape (core) from anhedral to euhedral, b) larger normally-zoned olivine-I crystal where thinness of overgrowth cannot change overall shape of original grain, and c) an array of olivine crystals including homogeneous smaller crystals *versus* crystals that show normal (lighter red) or reverse (darker red) zoning. Overgrowths are relatively homogeneous from crystal to crystal whereas core compositions are diverse. Yellow colours represent carbonate (orange is calcite); brighter shades are Mg-rich zones. False colours also identify serpentine mesostasis (black) and spinel microphenocrysts (white).

2.5 Olivine composition

2.5.1 Analytical methods

Quantitative elemental analysis of olivine was performed using the fully automated CAMECA SX-50 electron microprobe (Earth and Ocean Sciences, University

of British Columbia, Vancouver, Canada). Analytical conditions were 15.03 kV accelerating voltage, a 20.05 nA primary electron beam current, and peak and background counting times of 60 and 30 s respectively. We used a 5 μm beam diameter. For the thinnest rims on olivine a beam diameter of 1 μm was used, and count times were increased. The only minor elements detected were nickel and calcium. We analyzed 7 different samples (Table 2.1), comprising 85 point-analyses of cores of olivine-I grains and 36 of olivine-I rims, 97 of olivine-II cores, and 103 of olivine-II rims.

Thirty-two trace elements were analyzed by laser ablation inductively coupled plasma mass spectrometry (LA-ICP-MS). Analyses were made with a New Wave UP 213 Nd-YAG 213 nm UV laser ablation system coupled to a ThermoFinnigan Element2 single collector, high-resolution magnetic sector ICP-MS (Department of Geological Sciences, University of Manitoba, Winnipeg, Manitoba, Canada). The laser was operated at 10 Hz, which generated a laser flux of approximately 6 J/cm^2 with a 30-40 μm beam. For line profiles a beam diameter of 15 μm at 20 Hz at a scan speed of 2 μm/s was used. Calibration was performed using the National Institute of Standards (NIST) 610 glass standard, with silicon, previously determined by electron microprobe analysis, as an internal standard. The detection limit for LA-ICP-MS is below 0.1 ppm for most elements and in run precision is ~10%.

2.5.2 Variations within and between samples

Our analysis of compositional variations within olivine is based on recognizing and grouping analyses from 5 separate textural types of olivine in each sample: i) cores of olivine-I, ii) overgrowths of olivine-I, iii) cores of olivine-II, iv) overgrowths of olivine-II, and v) neoblastic olivine within microxenoliths of peridotite and dunite. Therefore, for

each of the 7 samples (Table 2.1), there are 5 separate bins of olivine composition. Statistical properties of the olivine compositions (Fo- and Ni-contents) for each bin are summarized in Table 2.2 (olivine-I) and Table 2.3 (olivine-II). Complete mineral composition analyses of all grains are in appendix B (CD).

We have treated the distribution of olivine compositions within each dataset as a normal distribution (cf. Appendix C). As such, each dataset is fully described by a mean and standard deviation allowing us to use the Students t-test for the equality of means. For example, we tested whether the means of the "olivine-II cores" were statistically the same for all 7 samples (cf. Nicholls and Russell, 1991 for review of hypothesis testing). Although the compositions of olivine-II cores for Samples 1 and 2 have different mean Fo ($Fo_{91.3}$ vs. $Fo_{91.1}$) and NiO contents (3600 vs. 3550 ppm; Table 2.3) they must be considered equivalent given the associated standard deviation of each population (Table 2.3 and 2.4). The results for each comparison are also listed in Appendix A (Table A2). Our analysis shows that the 5 textural-based groups of olivine compositions have statistically equivalent means across most of the samples. The equivalence of means between samples for the 5 textural-based sets of compositions allows us to combine the datasets from each of the 7 samples into 5 larger data-groups representing the 5 textural classes of olivine in all samples.

Table 2.2. Compositions of olivine-I for 5 coherent kimberlite samples based on N crystals reported as: mean ($\bar{x}$), standard deviation (1s), maximum, and minimum values of mole% forsterite and NiO content (ppm).

		1	2	3	4	5
Core	$\bar{x}_{Fo}$	91.3	91.3	91.8	91.4	91.8
	1s	0.9	0.9	0.9	0.9	1.7
	min	88.9	89.7	89.7	89.4	89.1
	max	92.5	92.9	93	92.9	93.2
	N	20	18	22	18	7
Rim	$\bar{x}_{Fo}$	91.0	91.1	91.2	91	90.8
	1s	0.4	0.2	0.5	0.3	1
	min	90.3	90.1	90.7	90.5	89.4
	max	91.3	91.4	92.1	91.3	92.3
	N	6	8	7	7	8
Core	$\bar{x}_{NiO}$	3550	3400	3400	3350	3100
	1s	550	400	450	550	600
	min	1900	2650	2500	2300	2200
	max	4600	4100	4000	4250	3800
	N	20	18	22	18	7
Rim	$\bar{x}_{NiO}$	1900	1650	2600	1500	2150
	1s	850	300	1100	300	500
	min	950	1050	1350	1100	1700
	max	3300	2100	3800	1900	3150
	N	6	8	7	7	8

Table 2.3. Compositions of olivine-II based on N crystals reported as: mean (`x), standard deviation (1s), maximum, and minimum values of mole% forsterite and NiO content (ppm).

		1	2	3	4	5	6	7
Core	$\bar{x}_{Fo}$	91.3	91.1	90.6	91.2	91.6	91.2	91
	1s	0.9	0.6	0.8	0.9	1	0.8	0.5
	min	89.6	90.2	88.7	90.2	90	90.1	90.3
	max	92.7	91.9	91.84	93.5	93.3	93	91.9
	N	12	13	14	19	13	15	11
Rim	$\bar{x}_{Fo}$	91.3	91.2	91.2	91.2	91.3	91.2	91.4
	1s	0.3	0.4	0.2	0.4	0.4	0.3	0.2
	min	91	90.8	90.9	90.6	90.9	90.6	91.1
	max	92	92.6	91.7	92.3	92.2	91.6	91.7
	N	10	17	15	20	14	16	11
Core	$\bar{x}_{NiO}$	3600	3550	3550	3300	3450	3650	3650
	1s	450	350	450	400	500	500	500
	min	2800	3000	2900	2650	2550	2850	2450
	max	4450	4050	4650	3950	4750	4350	4200
	N	12	13	14	19	13	15	11
Rim	$\bar{x}_{NiO}$	1500	1450	1800	2050	1700	2100	1450
	1s	450	500	850	1000	500	750	350
	min	850	800	700	800	1100	1200	850
	max	2400	3050	3750	4150	2600	4100	2150
	N	10	17	15	20	14	16	11

Table 2.4. Mean trace element contents (ppm) of olivine by LA-ICP-MS.

Element	Ol-II core	Ol-I core	Ol-II rim
Ca	261	259	326
V	6.57	5.43	6.03
Cr	263	167	392
Co	143	156	143
Ni	3141	3130	2727
Nb	0.18	0.22	0.41
La	0.030	b.d.l	0.198
Ce	0.030	b.d.l	0.292
Th	0.003	0.018	0.022
U	0.004	0.004	0.006

2.5.3 Olivine-I composition

We investigated the compositional differences between olivine-I cores and their overgrowths using the two pooled olivine-I datasets (i.e., cores vs. overgrowths; Figure 4). Our null hypothesis for the olivine-I datasets is:

Ho: The mean compositions for olivine-I cores and overgrowths are equal.

Rejection of **Ho** implies the alternate hypothesis:

Ha: The two sample populations have distinct means.

If **Ha** is accepted, then the mean compositions of cores and overgrowths are chemically distinct, and the two groups of olivine composition may require different origins.

In terms of distinguishing olivine-I overgrowths from their cores, we found Ni content to be the most effective. The composition of olivine-I cores varies from $Fo_{89\text{-}93}$ with a mean of Fo_{92} (Fig. 2.4a). The NiO content in the cores ranges from 1900 to 4600 ppm, and is centered on 3400 ppm (Fig. 2.4b). In comparison, the olivine-I overgrowths have an overlapping but more restricted range in Fo-content ($Fo_{90\text{-}92}$) and an average composition of Fo_{91} (Fig. 2.4c), and have nickel content in the overgrowths spans 950 to 3800 ppm.

A bimodal distribution is apparent in the nickel content of olivine-I overgrowths (Fig. 2.4d). There is a large peak present at ~1500 ppm and a smaller peak at ~3500 ppm. Since the smaller peak coincides with the mean core composition, it is likely that this peak results from analysis of overgrowths and some cores; i.e., it is an artifact due to the difficulty of sampling thin overgrowth (typically < 10 μm) material.

The variance of forsterite in the olivine-I rims (Fig 2.4c) is smaller (±0.6) compared to olivine-I cores (±1; Fig. 2.4a), whereas the variance of nickel content is greater in the rims (±1500 ppm; Fig. 2.4b) than in the cores (±1000 ppm) in olivine-I (Fig. 2.4d). In the case of cores and overgrowths for olivine-I, **Ho** is rejected in terms of Ni-content at the 95% confidence level (Ha is accepted). This implies that, although the olivine-I cores and overgrowths are statistically equivalent in Fo, they are distinct in terms of Ni content. This supports the idea that the overgrowths represent a distinct process relative to the cores. Refer to appendix A3 for results of hypothesis testing

Figure 2.4. Variations in chemical compositions of olivine

Variations in chemical compositions of olivine as mole % Fo and NiO content (ppm). Histograms of olivine compositions are prepared for: (a, b) cores of olivine-I; (c, d) rims of olivine-I; (e, f) cores of olivine-II; and (g, h) rims of olivine-II. The solid black lines represent model Gaussian distributions based on the calculated means and standard deviation of each data set.

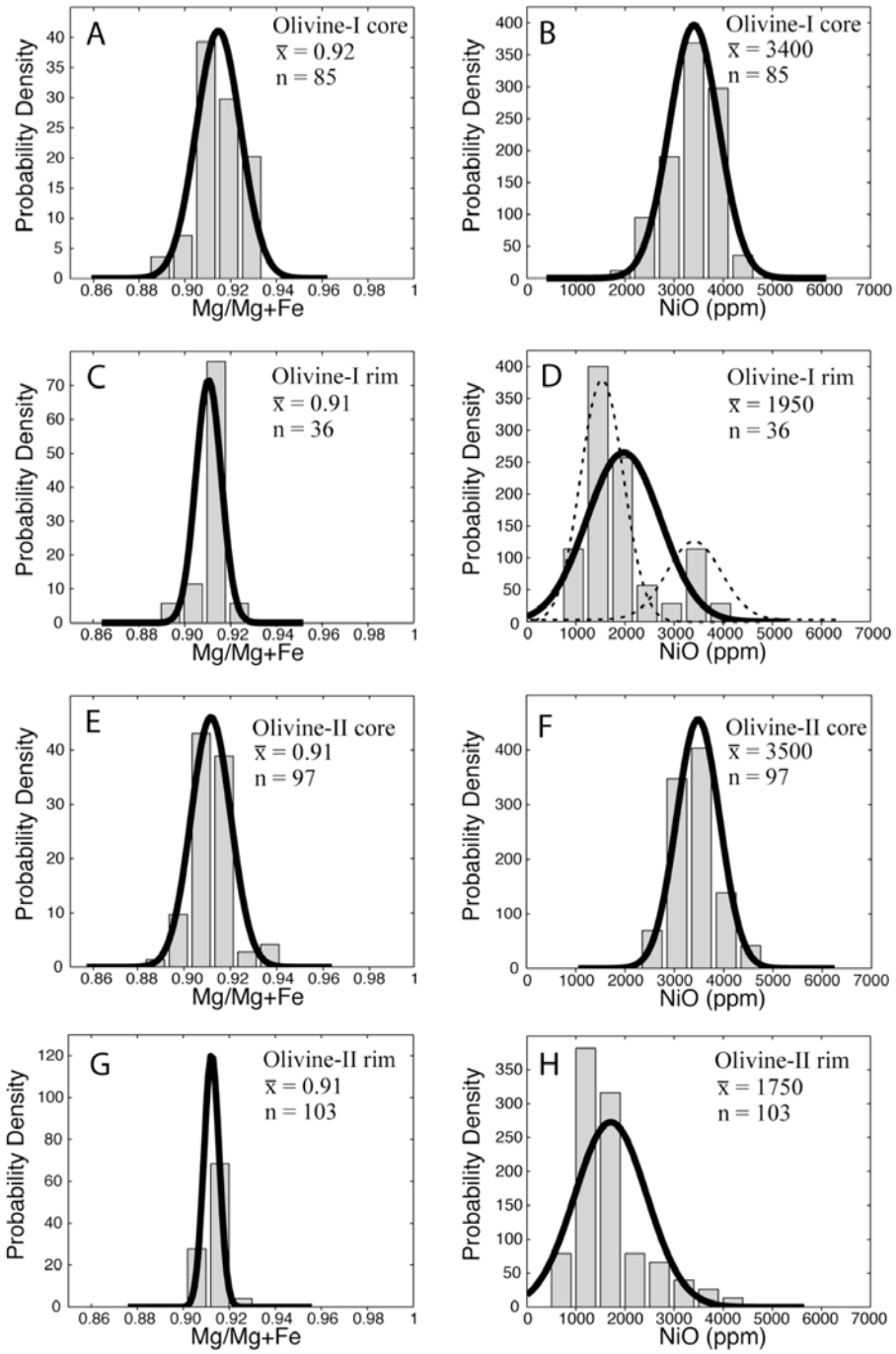

2.5.4 Olivine-II composition

We tested the olivine-II core and overgrowth datasets using the same method as described above (Fig. 2.4). Olivine-II core compositions vary from Fo_{89-94} with a mean of Fo_{91} (Fig. 2.4e), and the nickel content ranges from 2450 to 4750 ppm centered around 3500 ppm (Fig. 2.4f). The compositional range of olivine-II rims is $Fo_{91-93,}$ with a mean of Fo_{91} (Fig. 2.4g), which is a substantially smaller variability than forsterite in the cores (Fig. 2.4e). Sample variance of forsterite in olivine-II rims is again smaller (±0.3; Fig. 2.4e) compared to the variance of forsterite in olivine-II cores (±0.8; Fig. 2.4f). The nickel content in olivine-II rims ranges from 700 to 4150 ppm with a mean 1750 ppm (Fig 2.4h). In contrast to Fo-content, the variance in nickel content is much greater in the cores (±2800 ppm; Fig. 2.4f) than in the rims (±750 ppm; Fig. 2.4h).

A statistical analysis of the NiO content data requires rejection (95% confidence level) of the null hypothesis: **Ho**: The mean compositions of olivine-II cores and overgrowths are equal. This implies that the overgrowths to olivine-II are compositionally distinct from their cores and are likely to have formed by different processes. As found for olivine-I crystals, this result suggests that the cores and rims have distinct origins.

We further explored the geometry of trace elemental zoning in olivine-II crystals from core to rim. Specifically we have performed chemical traverses across the crystal shown in Figure 2.5 using, both, EMP (solid lines) and LA-ICP-MS (dashed symbols). The x-axis to Figures 2.5c and 2.5d corresponds to the traverse marked on the false coloured backscattered images shown in Figure 2.5a and 2.5b respectively. (c.f. Figure caption 2.3 for colour information). The EMP traverses show Ni content to decrease

sharply from ~3500 (Fig. 2.5c) and 4000 ppm (Fig. 2.5d) in the core to ~1500 ppm in the rim. Ca content increases at the core-overgrowth interface and is highest at the rim of the crystal (e.g. Fo-rich rind).

Figure 2.5c summarizes LA-ICP-MS results that show a similar zonation in NiO content (open circles) to that of the EMP analyses. Movement of the 30-micron laser across the core-rim boundary is characterized by a marked decrease in nickel content, and an increase in chromium and calcium. Calcium content (crosses) is rarely detectable in olivine, however is detected in the overgrowths. Chromium content is higher in rims (closed circles) than in cores (Fig. 2.5c, Table 2.4). On average, chromium increases from 260 ppm (olivine-II core) to 390 (olivine-II) rims.

Other trace element analysed by LA-ICP-MS include Ca, V, Cr, Co, Ni, Nb, La, Ce, Th and U. All of these elements are above detection in the rims of olivine-II. Ca, V, Cr, Co, Ni and Nb are all detectable in both olivine-I and II cores, whereas La, Ce, Th and U are below detection limits in cores and are only detectable in the rims (Table 2.4).

Figure 2.5. Chemical composition profiles for olivine-II crystals
Chemical composition profiles for olivine-II crystals. a) Back scattered image of olivine-II crystal (sample 1) showing orientation and length of electron microprobe traverse (white line), and LA-ICP-MS traverse (black line), b) Back scattered image of olivine-II crystal from sample 5 showing orientation and length of electron microprobe traverse (white line). The black dot on the white line marks major element zoning. (c & d) Electron microprobe traverse (solid black line) shows the sharp decrease in nickel content at the core-overgrowth interface.

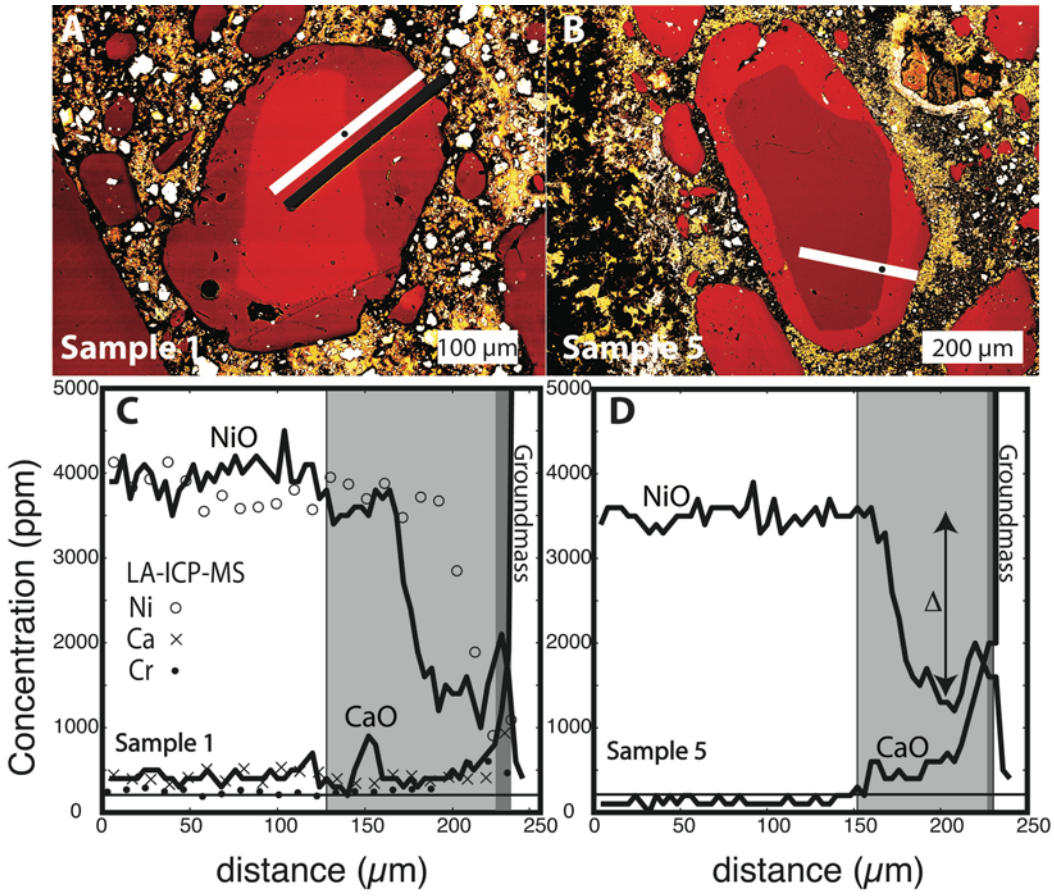

2.5.5 Composition of neoblastic olivine in microxenoliths

We have measured the composition of over 20 neoblasts from three microxenoliths, which are summarized in Figure 2.6b as the shaded Gaussian curves. The major and minor element compositions of neoblastic olivine in individual microxenoliths are homogeneous, but vary from xenolith to xenolith (Appendix B samples 1,3 and 5). The forsterite content in all samples ranges from (Fo_{90-92}), however over 90% of the grains analyzed are Fo_{91} in composition. Nickel content in neoblastic olivine is also

homogenous in any give nodule, but varies between samples. The lowest nickel content measured in neoblastic olivine is 2550 ppm, and most analyses are greater than 3000 ppm.

2.6 Origin of olivine

The results described above suggest that a simple xenolithic vs. phenocrystic origin does not accurately describe kimberlitic olivine. Figure 2.6a shows the model normal distributions of NiO content for the pooled datasets, and can be used to summarize the similarities and differences between olivine-I and olivine-II cores and overgrowths. These data clearly illustrate that the overgrowths on kimberlitic olivines are chemically distinct from their cores (Fig. 2.6a, 2.6c). More importantly, the cores of olivine-I and olivine-II have identical NiO contents, and the overgrowths of olivine-I and olivine-II have identical (but different from the cores) NiO contents (Fig. 2.6a, 2.6c). In Figure 2.6b the NiO contents for cores and overgrowths of olivine-I and olivine-II are pooled. These distributions are compared to the NiO contents of neoblastic olivine grains from 3 microxenoliths (Fig. 2.6b; shaded gray). The olivine neoblast compositions span the full compositional ranges found in olivine-I and olivine-II cores, but are compositionally distinct from the overgrowths on olivine-I and olivine-II grains (Fig. 2.6b). This comparison suggests that small, non-cored euhedral olivine grains could also derive from xenoliths of recrystallized mantle peridotite.

The Fo-contents of olivine cores presented in this study (Fig. 2.6; Table 2.2, Table 2.3) are fully consistent with a mantle origin, as reported for mantle samples around the world (Fo_{90-94}; Gaul et al., 2000; Griffin et al., 2003), as well as studies of the Slave Cratonic mantle (Fo_{91-94}; Kopylova and Caro, 2004; Griffin et al., 1999). Most olivine

compositions reported for mantle xenoliths (Sato 1977; Ryan et al. 1996; Griffin et al. 1989; Griffin et al. 1992; De Stefano et al. 2006) and xenocrysts in kimberlite (Fedortchouk & Canil 2004, Kamenetsky et al. 2008, Arndt et al. 2006) have NiO contents in excess of 3000 ppm. There are no studies reporting mantle olivine with nickel contents less than 2400 ppm. We therefore make the interpretation that all of the cores measured in this study (1900 to 4750 ppm; $\bar{x}$ = 3450) are mantle derived. This is critical because it implies that even most of the euhedral crystals (i.e., those having distinct cores) are mantle-derived and do not the result from crystallization of kimberlite magma.

The recrystallization processes that produced the neoblastic olivine (e.g., Paschier and Trouw, 2005) found in microxenoliths of peridotite provide an additional source for small euhedral crystals to appear "phenocrystic". Such grains are distinguished in kimberlite by their euhedral shape, size (< 1 mm), the absence of a discrete overgrowth, and NiO and Fo-contents indicative of a mantle origin (Fig. 2.6b).

In contrast to the cores, overgrowths on olivine-I and olivine-II are marked by the presence of mineral/fluid inclusions and associated with a major drop in NiO content (700 to 4150 ppm; $\bar{x}$ = 1850). These observations suggest a different origin for the overgrowths than ascribed to the olivine cores. The low NiO contents in the olivine overgrowths are inconsistent with a mantle source and best interpreted as resulting from crystallization of kimberlite melt onto pre-existing xenocrystic olivine.

In summary, we observe texturally and chemically distinct overgrowths on olivine-I (i.e. macrocrysts) and olivine-II (i.e. phenocrysts). The larger grains remain rounded in shape (Fig. 2.1a) because the overgrowths are thin relative to the diameter of the original olivine crystal. The smaller olivine grains are commonly subhedral to

euhedral in shape (i.e. idiomorphic) because the thickness of the overgrowths is sufficient to change the shape of the original grain (Fig. 2.1b). The cores of most olivine grains having discernible overgrowths are rounded to sub-rounded regardless of the size of the present olivine grain. Our analysis shows that overgrowths exist on all morphologies and sizes of olivine in kimberlite; there is little evidence to support exclusive homogeneous nucleation of olivine in kimberlite (i.e. true phenocrysts). Rather the smaller idiomorphic olivine population found in kimberlite results from heterogeneous crystallization of olivine onto activated surfaces offered by pre-existing, rounded, smaller (< 1 mm) xenocrysts of olivine. If much of olivine crystallization is heterogeneous, then this suggests that the amount of olivine that crystallized during transport and eruption has been greatly overestimated. Below we discuss the extent of olivine crystallization and its consequences.

Figure 2.6. Pooled olivine compositions
Differences in olivine compositions summarized in terms of NiO contents (ppm). a) Compositions of cores and rims of olivine-I (cartoon of rounded crystal) and olivine-II grains (cartoon of euhedral crystal). Shading of cartoons denotes part of crystal analyzed. Solid lines show Gaussian distribution curves for core and rim analyses from olivine-I grains; dashed lines correspond to analyses from olivine-II grains. b) Pooled compositional datasets for all cores and all rims of olivine grains (cf. Fig. 2.6a) shown as two separate curves. These curves are compared to compositions derived from three polycrystalline microxenoliths (shaded fields). c) Electron microprobe analyses of olivine from Diavik kimberlite plotted as mean NiO content (ppm) *vs*. mean Fo-content for olivine-I and olivine-II cores and rims (see text). Crosses indicate the 1s variation in each sample set and are compared to the mean analytical uncertainty (1s; upper right)

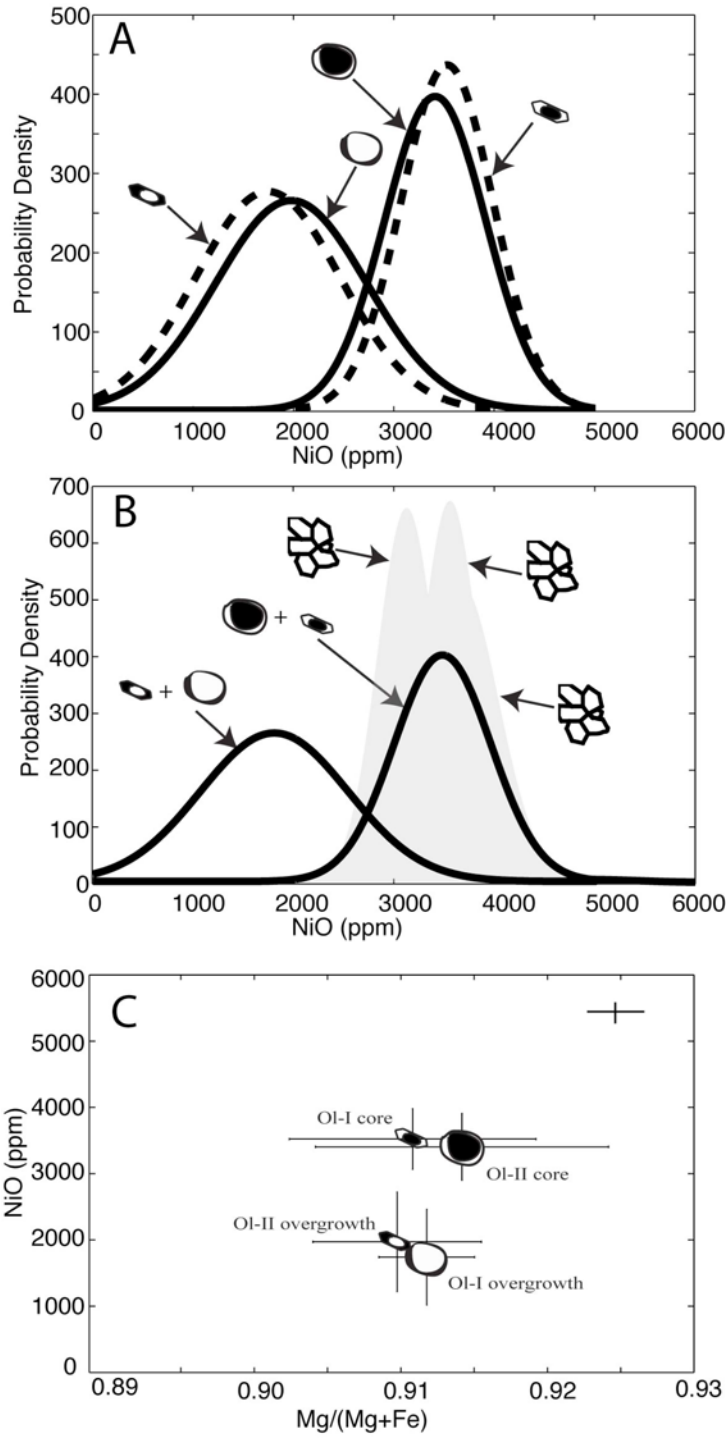

2.7 Discussion

2.7.1 Models for olivine growth

Renewed crystal growth on pre-existing mineral surfaces (heterogeneous crystallization) is commonly observed in volcanic rocks (e.g. Davidson et al. 2005; Ulianov et al. 2007). Davidson et al. (2005) suggest that the crystal 'cargo' (e.g., larger crystals) within many intermediate magmas are not true phenocrysts (i.e., derived form the host melt), but, rather, are commonly inherited by the magma from other sources and modified by subsequent crystallization.

Previous studies have suggested that overgrowths on preexisting crystals can: 1) be the same thickness regardless of the size of the original crystal (constant thickness; e.g., Kretz, 1966; Carlson et al., 1995), 2) have varying thicknesses resulting from equal volumes of growth being assigned to each original crystal (equal volume; e.g. Tiller 1991), or 3) have varying thicknesses that are proportional to the surface area of the original crystal (surface area controlled; e.g. Kile & Eberl 2003; Kouchi et al., 1986). Here, we model these three end-member modes of overgrowth crystallization in order to reconstruct the abundance and size of olivine in our kimberlite samples prior to crystallization. In this way we are able to constrain the extent (e.g., volume %) of crystallization during kimberlite ascent.

Our modeling is based on olivine crystal size distribution (OSD) data collected from a polished slab and thin section of kimberlite. The OSD includes all olivine grains having a cross-sectional area of 6.2×10^{-4} to 36.3 mm^2. The OSD comprises 24,446 particles of olivine that comprises 44 volume % of the sample. OSD quantification and

the image analysis methods are fully described by Moss et al., (2008) and Holden et al., (2008).

The model solution also depends on limits derived from petrographic observation, including: a) observed overgrowth thicknesses never exceed 120 μm, and b) the largest euhedral crystals lacking discrete overgrowths are ~300 μm in diameter. We assume that the current observed olivine size distribution (OSD) represents the combination of original xenolithic olivine, plus the crystallized overgrowths. The model will also return an, a priori unknown, but calculated fraction of newly nucleated and grown olivine crystals; these are true phenocrysts resulting from homogeneous crystallization.

2.7.2 Model A: Constant thickness

Many authors have discussed models for crystallization that produce constant thicknesses of overgrowths on pre-existing crystals (Kretz 1966; Carlson et al., 1995; Nielson, 1964; Kirkpatrick, (1981); Lasaga, 1998). Most of these growth models are based on growth rates independent of crystal size. We have modeled crystallization of olivine in our kimberlite according to this stricture by reducing the size of each olivine in the OSD by a constant thickness. Figure 2.7a plots the present size (radius) of olivine grains against the model radial growth thickness. The thick, solid-grey, horizontal line represents the growth thickness modeled as a constant and prescribed by the observed maximum 120 μm growth thickness. This scenario suggests an ideal olivine crystallization volume (Vx) of ~10% in the system, and imposes a maximum phenocryst radius of 120 μm. A consequence of this model is that smaller crystals (<120 μm) are too small to accommodate such a large decrease in their radius without being consumed completely. The 1:1 line represents the model results for these smaller crystals, where the

model growth thickness exactly equals the observed crystal radius. These two curves intersect (vertical dashed line) and define the population of crystals supporting heterogeneous crystallization of overgrowths (to the right) and the population that were produced by homogeneous nucleation (to the left; Fig. 2.7d). Our preferred model (i.e., 10% crystallization) supports minimal homogeneous growth, where >95% olivine crystallization is heterogeneous (Fig. 2.7d). For comparison, model lines are present for 2, 5 and 15% olivine crystallization by volume (horizontal dashed lines). The model line representing 15% olivine crystallization requires a growth thickness of 190 μm on each crystal and is not supported by observation. Smaller amounts of crystallization under the constant thickness stricture can produce only very thin overgrowths and predict very small phenocryst sizes (<< 120 μm radius).

2.7.3 Model B: Constant volume

The constant volume model requires an equal volume of olivine to be subtracted from each crystal (Fig. 2.7b). The constant volume assigned to each crystal will produce unique 'overgrowth thicknesses' because of the different sizes of the original seed crystals. In this model, larger crystals have thin overgrowths, and smaller crystals have thicker overgrowths. The thick, solid grey line represents 1% olivine crystallization of the system, which best matches the limiting value of observed overgrowth thickness (120 μm). In the case where the volume to be subtracted from the crystal is greater than the volume of the crystal, we identified the grain as a bona fide phenocryst (homogeneous growth). The 1:1 line represents homogeneous crystal growth, that is, the growth thickness is the same as the measured radius of the crystals. These two lines intersect and define (for 1% crystallization (Vx)) the population of crystals that would have

overgrowths (to the right of the intersection) and the population that were produced by homogeneous nucleation (to the left of the intersection). For comparative purposes we have modeled the effects of greater amounts of crystallized olivine. If 5 % of the original system crystallized to produce olivine, the model predicts homogeneous growth up to 500 μm in radius. Thicknesses greater than 120 μm (i.e. >1% crystallization; shaded area) are not petrographically supported because we do not observe overgrowths larger than 120 μm. The optimal model (1% crystallization) requires small volumes (< 0.03 mm^3) of olivine added to each crystal. It also requires sub equal amounts of homogeneous (0.55%) vs. heterogeneous (0.45%) crystallization of olivine (Fig 2.7d).

2.7.4 Model C: Surface area controlled

Our last model assumes that the surface area of the original olivine grain dictates the proportion of new crystallization. Specifically, the total amount of olivine crystallization is distributed equally over the total surface area represented by all pre-existing olivine grains. The surface areas (total and individual) at the onset of crystallization are unknown and, thus, have to be modeled iteratively until there is a fit between the current OSD, the model original OSD, and the total amount of new crystallization.

The model results are summarized in Fig 2.7c and the thick grey line represents the growth thicknesses vs. original radius for 5% olivine crystallization. This model amount of crystallization is deemed optimal because it produces no overgrowths larger than 120 μm. A consequence of this model is that, once again, some crystals are too small to allow a surface area controlled overgrowth. The 1:1 line represents such crystals, which are treated as products of homogeneous crystallization. In this model,

homogeneous and heterogeneous OSD components are marked by the vertical dashed line connecting the dark curve (to the right) and the 1:1 line (to the left). This implies a maximum phenocryst radius of 120 μm.

Our optimal model allows for 5% crystallization of olivine and predicts thinner overgrowths than the previous models. Consequently, this model ascribes smaller volumes of olivine to homogeneous crystallization (< 0.5%); most of the olivine crystallization is attached to pre-existing crystal surfaces (~ 4.5 %; Fig. 2.7d). The surface area growth model causes smaller original crystals to have thin overgrowths and larger crystals to have thick overgrowths.

For comparative purposes we have modeled the effects of greater extents of olivine crystallization. For 10% olivine crystallization of the system, the model predicts homogeneous growth up to 380 μm, and overgrowth thicknesses to a maximum of 380 μm. However, euhedral crystals of this size (380 μm) are always observed to have cores, and overgrowth thicknesses greater than 120 μm (i.e. >5% crystallization; shaded area) are not supported petrographically. This model does not support smaller amounts of crystallization (i.e. < 5%) because the homogeneous crystal sizes and overgrowth thicknesses would be smaller than petrographically observed.

In order to test which of the above models is described by growth in natural samples we examined full BSE thin section scans of coherent kimberlite. High-resolution BSE scans were merged for an entire thin section. The contrast of the image was adjusted to amplify forsterite-zoning patterns in olivine. The image was then printed on a 42 by 76 inch size paper at 85 dpi resolution enabling identification of zoning patterns in olivine down to 0.08 mm diameter. A 25 by 25 cm grid was placed on the entire image (28

squares in total). Major and minor axes were measured for olivine in each grid square that had discernable overgrowths. The thickest and thinnest rim thicknesses were measured for each grain and averaged. The observed average crystal diameter vs. the apparent rim thickness is presented for a total of 95 grains in Appendix E. The results show that larger crystals have thicker overgrowths than smaller crystals. These results are inconsistent with the constant thickness (A) and constant volume (B) models. Growth thicknesses modeled by surface area activated growth (C) is, however, permissive with these results.

Surface area controlled crystallization is our preferred model because: a) it is consistent with measured thickness of overgrowths, b) the model is consistent with observations of maximum phenocryst sizes and overgrowth thicknesses in kimberlite and, c) this style of crystallization has been shown experimentally to be dominant in stirred systems (e.g. Kile & Eberl 2003; Eberl et al., 2002). This implies that a maximum of 5% olivine crystallization has occurred, and that the volume of olivine growth is dominantly present as overgrowths on xenocrystic olivine cores. This reduced estimate of olivine crystallization departs from the going paradigm that kimberlite contains 25% phenocrysts (e.g. Mitchell, 2008; Scott Smith, 1996), and has consequences for kimberlite melt chemistry and orthopyroxene dissolution.

Figure 2.7. Models for crystallization of olivine in kimberlite

Model output is plotted as observed radius vs. overgrowth thickness for: a) the constant thickness model, b) the constant volume model, and c) the surface area controlled model. The white areas denote solutions consistent with observations; preferred solutions indicated by the solid grey lines. Dashed lines show less feasible solutions. Numbers on vertical lines represent the model maximum diameter of the largest phenocryst for each model. Vx is the volume of crystallized olivine. d) Differences between the models are summarized as a bar graph showing volume % of heterogeneous vs. homogeneous olivine crystallization.

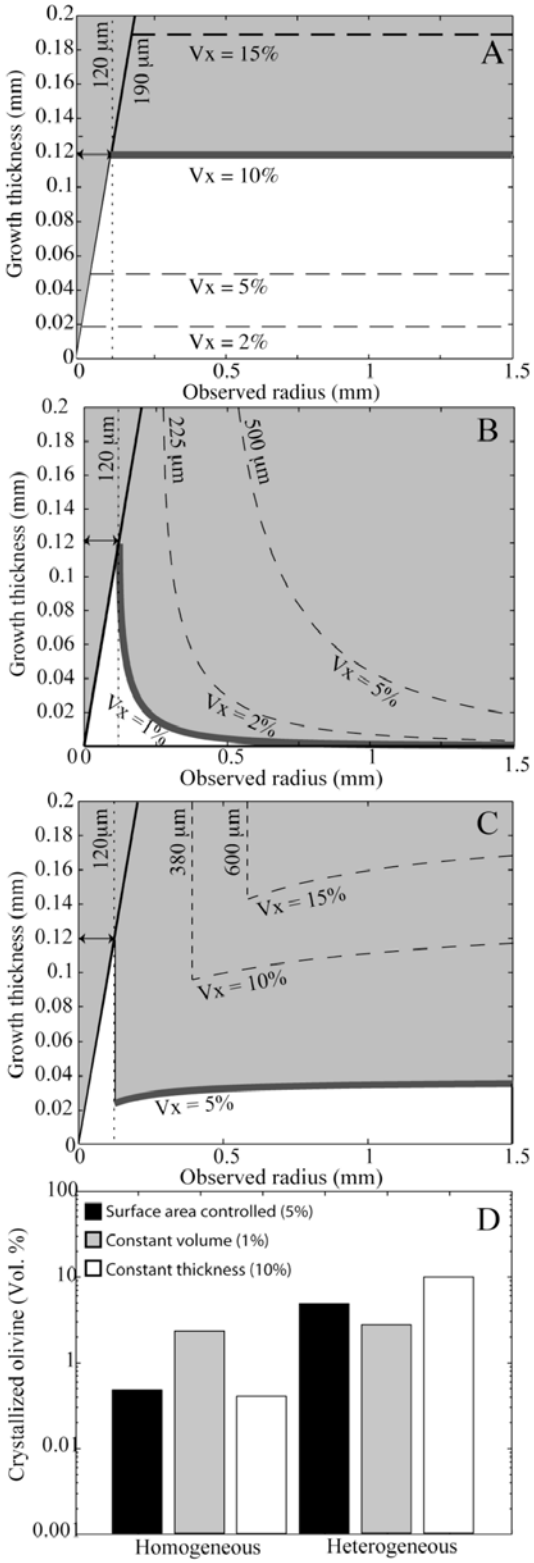

2.7.2 Importance for primitive kimberlite melts

Generally, estimates of primitive kimberlite melt compositions are obtained by isolating and analysing fine grained, quenched kimberlite found at country rock-kimberlite contacts (e.g., chill margins; Price et al., 2000). A recent example of this approach is afforded by the work of Kopylova et al., (2007) who measured the bulk composition of samples of aphanitic ('macrocryst-free'), vesiculated kimberlite from the Jericho kimberlite. The bulk composition estimate was based on a chemical point counting technique, which created a liquid composition from the proportions and identities of groundmass phases and the proportion and composition of olivine phenocrysts (Fo_{91}). Kopylova et al., (2007) considered these measurements as representative of the composition of the primitive kimberlite melt. On this basis the reconstructed primitive kimberlite melt composition for the Jericho kimberlites was predicted to have an Mg# of 87.3. However, Kopylova et al. (2007) noted that the olivine in equilibrium with this melt was expected to have a substantially higher forsterite content ($Fo_{95;}$ assuming a $K_D^{Fe\text{-}Mg}$ of 0.36; Herzberg and O'Hara, 2002), than observed in the phenocrystic olivine (Fo_{91}). The discrepancy was recognized and clearly discussed by the authors, but no explanation was found.

One by-product of Kopylova et al. (2007)'s computer-assisted image analysis of SEM microphotographs is that they have well-measured modal proportions (~27% by volume) of what they consider "phenocrystic" olivine (cf. Kopylova et al., 2007). Given our analysis, it is possible that Kopylova et al.'s (2007) modal proportion of olivine (i.e., 27 vol.%) is an overestimation of the amount of olivine crystallized from the Jericho kimberlite; much of the phenocrystic olivine (e.g., cores) may actually be xenocrystic.

The assumption that all of the observed olivine phenocrysts are products of melt crystallization causes an overestimation of the magnesium number of the reconstructed primitive melt and implies more forsteritic olivine phenocrysts than observed.

Our work provides a simple means to partially reconcile Kopylova et al.'s (2007) results and calculations because we have shown that the smaller, euhedral population of olivine grains (olivine-II) comprises both a core of xenocrystic olivine, and an overgrowth of newly crystallized material. This suggests that a relatively small fraction of the 27 vol.% olivine phenocrysts can be ascribed to crystallization of the kimberlite melt. Indeed, we would suggest that olivine crystallization might actually be closer to 5 vol. %, and that the remaining olivine (22%) is actually xenocrystic.

Recalculation of their melt composition by subtracting 22% of the olivine (i.e., xenocrysts of Fo_{94}) from their melt composition reduces the Mg# from 87.3 to 83.6, and reduces the equilibrium olivine composition from Fo_{95}, to $Fo_{93.5}$. This modified estimate represents the magma composition comprising melt plus 5 vol. % olivine (phenocrysts); based on K_D of 0.36 the melt would have an Mg# of 82.6 and be just saturated with ~Fo_{93} olivine. Although our model reduces the Mg# and predicted phenocryst compositions, the predicted olivine composition remains 2 mol% higher than observed (e.g., Fo_{93} vs. Fo_{91}).

2.7.3 The dissolution of orthopyroxene

The ratio of mantle derived orthopyroxene to olivine macrocrysts is low in kimberlite relative to the ratio of orthopyroxene to olivine in Cratonic mantle xenocrysts (e.g. Kopylova et al., 2007). The relatively low abundance of orthopyroxene in kimberlite has been ascribed to rapid dissolution of orthopyroxene in the kimberlite melt during transport (Luth, 2007; le Roex et al., 2003; Ulmer and Sweeney, 2002). Estimates of the

amount of orthopyroxene assimilated by the kimberlite melt are as high as 25 vol. % (Mitchell, 2008; Le Roux et al., 2003; Kopylova et al., 2007). Several experimental (e.g. Edgar et al., 1993) and theoretical studies show that orthopyroxene is the unstable of the peridotitic mantle minerals in kimberlite melt. A possible explanation is that orthopyroxene dissolution is balanced, in terms of molar amounts and enthalpy, by a concomitant crystallization of olivine (Mitchell, 1995). This suggestion has the merit of providing a possible explanation for the paucity of orthopyroxene xenocrysts in kimberlite, and would permit large volumes of olivine crystallization during the rapid ascent of kimberlite.

We have modeled several different reaction paths involving assimilation of orthopyroxene and olivine crystallization (Fig. 2.8) to highlight the repercussions of reduced olivine crystallization. We modeled the reaction paths using MELTS (Ghiorso and Sack, 1995) at a pressure of 10 Kb using an average model estimate of kimberlite melt composition. We suppressed all solid phases from crystallizing except for olivine, while forcing assimilation of orthopyroxene and the calculations were performed such that the mass of original melt and assimilated orthopyroxene summed to 100 grams of new melt. Our petrographic estimates are in vol.% but were converted to mass % equivalents for purposes of comparison.

For reference, we have modeled the crystallization path of olivine without orthopyroxene assimilation and shown it as Case 1 (Fig. 2.8a; thin black line). The model path starts at liquidus conditions (1569ºC) and produces 5 wt.% olivine crystallization after a ~40°C decrease in temperature. Isobaric crystallization of 25 wt.% olivine requires 200°C cooling. Figure 2.8b shows temperature vs. the net change in enthalpy of the

Figure 2.8. Models for assimilation of orthopyroxene

Models for assimilation of orthopyroxene by kimberlite melt and concomitant olivine crystallization. End-member models include (1) olivine crystallization (thin black curve), (2) the 1:1 molar reaction of orthopyroxene assimilation to olivine crystallization (thick grey curve), and (3) assimilation of a fixed amount (27.5 g) of orthopyroxene supported by varying amounts olivine crystallization (thick black curve). a) T (^{o}C) *vs*. olivine crystallization (wt. %); horizontal grey line denotes our model estimate of olivine crystallization (~ 5%), b) T(^{o}C) *vs.* the change in system enthalpy for each model path contoured for different amounts of orthopyroxene assimilation and olivine crystallization (thin black contours), and c) compositions of melts (SiO_2 and Mg#) produced along each model path normalized to the original melt composition. For reference we also show the initial melt liquidus (dashed vertical line) and the specific masses of each mineral consumed or crystallized along the model (labeled dots). Arrows denote process direction.

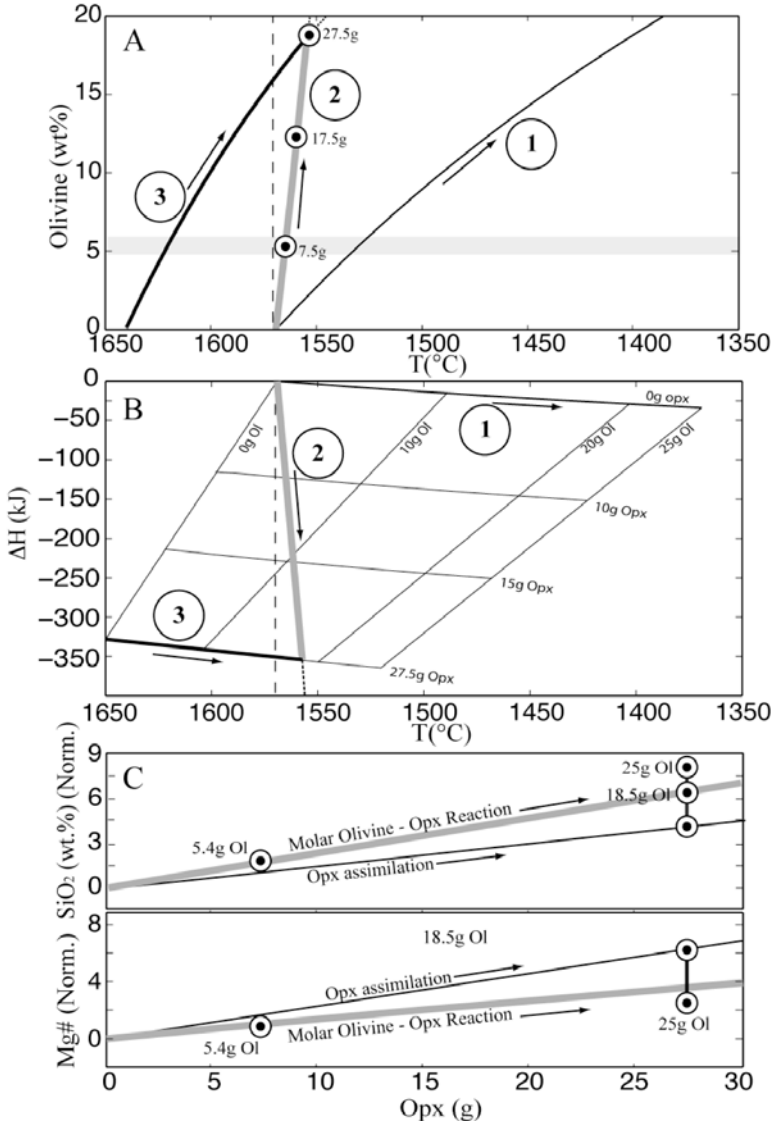

system between each step along the reaction path and the original state (i.e. prior to crystallization or assimilation). It is contoured for orthopyroxene assimilation and olivine

crystallization. The thin black line represents the olivine crystallization path. The system loses enthalpy by cooling (sensible heat) and shedding heats of crystallization (latent heat) in order to crystallize olivine. This crystallization path enriches the residual melt in SiO_2 whilst reducing the Mg# of the melt.

Figure 2.8 contains two additional reaction paths that show the effects of orthopyroxene assimilation. The first (Case 2) involves a mole for mole, fully coupled assimilation of orthopyroxene and crystallization of olivine (case 2; thick grey line)

$$Mg_2Si_2O_{6(S)}^{Opx} \Leftrightarrow Mg_2SiO_{4(S)}^{Ol} + SiO_{2(M)}$$

Case 2 couples orthopyroxene assimilation to olivine crystallization and serves as a vehicle to produce more silica rich melts whilst conserving enthalpy and minimizing cooling. However, the reaction implies that if 27.5 wt.% (i.e. 25 vol.%) of orthopyroxene was assimilated, ~18 vol.% olivine would is produced. This is not supported by our observations and volume estimations. The model can only allow for 7.5 g of orthopyroxene assimilation based on our estimates of olivine crystallization (5 vol.%) under this stricture. The enthalpy of the system (Fig. 2.8b) is nearly balanced for this reaction, and little cooling of the system is needed in order to keep the reaction molar (5ºC). Compositional modification of the kimberlite melt is only minor for this case, where if 5.4g (5 vol.%) of olivine is allowed to crystallize, the melt composition is enriched in SiO_2 and Mg# by 1 wt.% and +1 Mg# respectively.

The second model considers the case where a fixed amount (25 vol.%) of orthopyroxene is assimilated, and variable (0 to 30 vol. %) amounts of olivine crystallize. This case requires super-liquidus initial conditions (case 3; thick black line). Case 3 forces 25 vol. % orthopyroxene assimilation and, if there is no concomitant olivine

crystallization, requires the initial system to be ~100°C super-liquidus (Fig. 2.8a; heavy black line). Olivine crystallization (exothermic) can partially offset the enthalpy reduction due to orthopyroxene assimilation such that increased olivine crystallization allows for lower initial magma temperatures (i.e., less super-liquidus; Fig. 2.8b). System enthalpy decreases for each additional amount of orthopyroxene assimilated; the decrease in enthalpy is mitigated somewhat by olivine crystallization as indicated by the contours of olivine content (Fig 2.8b). For example assimilation of 27.5 g of orthopyroxene causes a 325 kJ reduction in enthalpy and requires the initial magma to be 100°C super-liquidus relative to olivine crystallization. However, if 15 g of olivine is allowed to crystallize the system enthalpy is reduced only by ~215 kJ (Fig. 2.8b) and the initial magma need not be super-liquidus (Fig. 2.8a).

For 27.5 g (25 vol. %) of orthopyroxene assimilation, case 3 predicts the melt to become enriched in SiO_2 (~4 wt.%), and increases the Mg# by ~4 times black vertical line (Fig. 2.8c). This model implies that the assimilation of orthopyroxene contributes a substantial component of the melts silica content (i.e. ~13% of the total silica).

In summary, using our estimates of olivine crystallization (5 vol. %) orthopyroxene can either; A) be assimilated by reduced amounts (7 vol. %) if the 1:1 molar reaction of orthopyroxene and olivine is obeyed (c.f. Mitchell, 1995) or, B) 25 vol. % orthopyroxene assimilation can be accommodated only if it is introduced to the melt at super liquidus conditions (i.e. +100°C). If the first scenario (A) is accepted it implies that olivine crystallization happened contemporaneously with the assimilation of orthopyroxene. The stability of orthopyroxene is shown to be unstable down to mantle depths in a kimberlite melt (c.f. Luth, 2007). This scenario then allows for olivine

crystallization to occur at great depths. If (B) is accepted, significant quantities of orthopyroxene have to assimilate in order to cool the melt to reach its liquidus. The time required to cool the melt allows the melt to ascend to crustal levels before olivine saturates the melt. The later model is our preferred model because of petrographic evidence that supports substantial amounts of transport before the onset of heterogeneous crystallization.

2.8 Summary

Olivine in kimberlite dominantly results from heterogeneous crystallization (<5 %) of olivine onto xenocrystic olivine derived from disaggregated mantle peridotite and a minor (< 0.5%) amount of homogeneous crystallization. Crystallization of overgrowths on rounded olivine xenocrysts traps melt, fluid and solid phases. Our reduced estimates of olivine crystallization provide a means to modify previous estimates of primitive kimberlite melt compositions so that they are reconciled with measured phenocryst compositions. If olivine crystallization and orthopyroxene dissolutions are strictly coupled, then the extent of orthopyroxene assimilation during transport is restricted to < 7%. If large (~25%) amounts of orthopyroxene assimilate during transport then kimberlite melts must begin their transit at super-liquidus (>100°C) conditions. Our analysis also suggests that care must be taken when we use modes and compositions of phenocrystic olivine to reconstruct primitive kimberlite melt compositions. The focus should be on recognizing, isolating and analysing true magmatic overgrowths rather than xenocrystic material. Likewise, zoning on large macrocrysts is due to olivine crystallization and care must be taken to distinguish these from diffusive profiles that denote other processes.

2.9 List of references

Arndt, N.T., Boullier, A.M., Clement, J.P., Dubois, M., Schissel, D., 2006. What olivine, the neglected mineral, tells us about kimberlite petrogenesis. eEarth, 1, 15-21.

Boudier, F., 1991. Olivine xenocrysts in picritic magmas: An experimental and microstructural study. Contributions to Mineralogy and Petrology, 109, 114-123.

Carlson, W.D., Denison, C., and Ketcham, R.A., 1995. Controls on the nucleation and growth of porphyroblasts: kinetics from natural textures and numerical models. Geological Journal, 30, 207–225.

Caro, G., Kopylova, M.G., 2004. The hypabyssal 5034 kimberlite of the Gahcho Kue cluster, southeastern Slave Craton, Northwest Territories, Canada: A granite-contaminated group-I kimberlite. The Canadian Mineralogist, 42, 183-207.

Clement, C.R., 1982. A comparative geologic study of some major kimberlite pipes in the Northern Cape and Orange Free State. Ph.D. Thesis. Department of Geology, University of Cape Town.

Clement, C. R., Skinner, E. M. W., and Scott, B. H. 1977. Kimberlite redefined. 2nd International Kimberlite Conference, Santa Fe, NM, Expanded Abstracts.

Davidson, J.P., Hora, J.M., Garrison, J.M., Dungan, M.A., 2005. Crystal forensics in arc magmas. Journal of Volcanology and Geothermal Research, 140, 157-170.

Dawson, J.B., 1994. Quaternary kimberlitic volcanism on the Tanzania Craton. Contributions to Mineralogy and Petrology 116, 473–485.

De Stefano, A., Lefebvre, N., Kopylova, M., 2006. Enigmatic diamonds in Archean calc-alkaline lamprophyres of Wawa southern Ontario, Canada. Contributions to Mineralogy and Petrology, 151, 158-173.

Eberl, D.D., Kile, D.E., Drits, V.A., 2002. On geological interpretations of the crystal size distributions: Constant vs. proportionate growth. American Mineralogist, 87, 1235-1241.

Edagar, A.D., Charbonneau, H.E., 1993.Melting experiments on a SiO_2-poor, CaO-rich aphanitic kimberlite from 5-10 GPa and their bearing on sources of kimberlite magmas. American Mineralogist, 78, 132-142

Fedortchouk, Y., Canil, D., 2004. Intensive variables in kimberlite magmas, Lac de Gras, Canada and implications for diamond survival. Journal of Petrology, 45 1725-1745.

Gaul, O.F., Griffin, W.L., O'Reilly, S.Y., Pearson, N.J., 2000. Mapping olivine composition in the lithospheric mantle. Earth and Planetary Science Letters, 182, 223-235.

Ghiorso, M.S., Sack, R.O., 1995. Chemical mass transfer in magmatic processes. IV. A revised and internally consistent thermodynamic model for the interpolation and extrapolation of liquid-solid equilibria in magmatic systems at elevated temperatures and pressures. Contributions to Mineralogy and Petrology, 119, 197-212.

Graham, I., Burgess, J.L., Bryan, D., Ravenscroft, P.J., Thomas, E., Doyle, B.J., Hopkins, R., Armstrong, K.A., 1998. Exploration history and geology of the Diavik kimberlites, Lac de Gras, Northwest Territories, Canada. In: Gurney, J.J., Gurney, J.L., Pascoe, M.D., Richardson, S.H. (Eds.), Proceedings of the VIIth International Kimberlite Conference. Red Roof Design, Cape Town, South Africa, pp. 262–279.

Griffin, W.L., Gurney, J.J., Ryan, C.G., 1992. Variations in trapping temperatures and trace elements in peridotite-suite inclusions from African diamonds: evidence for two inclusion suites, and implications for lithosphere stratigraphy. Contributions to Mineralogy and Petrology, 110, 1-15.

Griffin, W.L., Doyle B.J., Ryan, C.G., Pearson, N.J., O'Reilly, S.Y., Davies, R., Kivi, K., Van Achterbergh, E., Natapov, L.M., 1999. Layered mantle lithosphere in the Lac de Gras area, Slave Craton: Composition structure and origin. Journal of Petrology, 40, 705-727.

Griffin, W.L., O'Reilly, S.Y., Abe, N., Aulback, S., 2003. The origin and evolution of Archean lithospheric mantle. Precambrian Research, 121, 19-41.

Harris, M., le Roex, A., Class, C., 2004. Geochemistry of the Uinjiesberg kimberlite, South Africa: petrogenesis of an off-craton, group I, kimberlite. Lithos, 74, 149-165.

Herzberg C., and O'Hara M. J., 2002. Plume-associated ultramafic magmas of

Phanerozoic age. Journal of Petrology, 43, 1857–1883.

Holden, E.J., Moss, S., Russell, J.K., Dentith, M.C., 2008. An image analysis method to determine crystal size distributions of olivine in kimberlite. Computational Geosciences, (in press).

Kamenetsky, V.S., Kamenetsky, M.B., Sobolev, A.V., Golovin A.V., Demouchy, S., Faure, K., Sharygin V.V., Kuzmin, D.V., 2008. Olivine in the Udachnaya-East Kimberlite (Yakutia, Russia): Types, compositions and origins. Journal of Petrology, 49, 823-839.

Kennedy, L.A., Russell, J.K., Kopylova, M.G., 2002. Mantle shear zones revisited: The connection between the cratons and mantle dynamics. Geology, 30, 419-422.

Kile, D.E., Eberl, D.D., 2003. On the origin of size-dependent and size-independent crystal growth: Influence of advection and diffusion. American Mineralogist, 88, 1514-1521.

Kirkpatrick, R.J., 1981. Kinetics of crystallization of igneous rocks. In A.C. Lasaga and R.J. Kirkpatrick, Eds., Kinetics of Geochemical Processes, 8, 321–398. Reviews in Mineralogy, Mineralogical Society of America, Washington, D.C.

Kopylova, M.G. & Caro, G., 2004. Mantle xenoliths from the southeastern Slave Craton: Evidence for chemical zonation in a thick, cold lithosphere. Journal of Petrology, 45, 1045-1067.

Kopylova, M.G., Matveev, S., Raudsepp, M., 2007. Searching for parental kimberlite melt. Geochimica et Cosmochimica Acta, 71, 3616-3629.

Kouchi, A., Tsuchiyama, A., Sunagawa, I., 1986. Effect of stirring on crystallization kinetics of basalt: texture and element partitioning. Contributions to Mineralogy and Petrology, 93, 429-438.

Kretz, R., 1966. Grain-size distribution for certain metamorphic minerals in relation to nucleation and growth: Journal of Geology, 74, 147–173.

Lasaga, A.C., 1998, Reaction kinetics in geosciences: Princeton, New Jersey, Princeton University Press, 811 p.

Le Roex, A.P., Bell, D.R., Davis, P., 2003. Petrogenesis of Group I kimberlites from Kimberley, South Africa: evidence from bulk rock geochemistry. Journal of

Petrology 44, 2261–2286.

Li, T.S., Livk, I., Ilievski, D., 2003. Supersaturation and temperature dependency of gibbsite growth in laminar and turbulent flows. Journal of Crystal Growth, 258, 409-419.

Mitchell, R.H., 1970. Kimberlite and related rocks – a critical reappraisal. Journal of Geology, 78, 686-704.

Mitchell, R.H., 1986. Kimberlites: Mineralogy, Geochemistry, and Petrology. Plenum Press, New York.

Mitchell, R.H., 1995. Kimberlites, Orangeites, and Related Rocks. Plenum Press, New York.

Mitchell, R.H., 2008. Petrology of hypabyssal kimberlites: Relevance to primary magma compositions. Journal of Volcanology and Geothermal Research, 174, 1-8.

Moss, S., Russell, J.K., Andrews, G.D.M., 2008. Progressive infilling of a kimberlite pipe at Diavik, Northwest Territories, Canada: Insights from volcanic facies architecture, textures, and granulometry. Journal of Volcanology and Geothermal Research, 174, 103-116.

Nicholls, J., Russell, J.K., 1991. Major-element chemical discrimination of magma-batches in lavas from Kilauea volcano, Hawaii, 1954 – 1971 eruptions. Canadian Mineralogist, 29, 981-993.

Nielsen, A.E. (1964) Kinetics of Precipitation. Pergamon, New York.

Passchier, C.W., Trouw, R.A.J., 2005. Microtectonics, 2nd edition. Springer.

Price, S.E., Russell, J.K., Kopylova, M.G., 2000. Primitive magma from the Jericho pipe, N.W.T., Canada: Constraints on primary kimberlite melt chemistry (41) 6, 789-808.

Ross, J.V., 1983. The nature and rheology of the cordilleran upper mantle of British Columbia: Inferences from peridotite xenoliths. Tectonophysics, 100, 321-357.

Ryan, C.G., Griffin, W.L., Pearson, N.J., 1996. Garnet geotherms: Pressure-temperature data from Cr-pyrope garnet xenocrysts in volcanic rocks. Journal of Geophysical Research, 101, 5611-5625.

Sato, H., 1977. Nickel content of basaltic magmas: identification of primary magmas and a measure of the degree of olivine fractionation. Lithos, 10, 113-120.

Scott Smith, B.H., 1996. Undersaturated alkaline rocks: mineralogy petrogenesis, and economic potential. Mitchell, R.H. (ed.). Mineralogical Association of Canada, short course series. Winnipeg, Manitoba 1996.

Skinner, E.M.W., Clement, C.R., 1979. Mineralogical classification of southern African kimberlites. In: Boyd, F.R., Meyer, H.O.A. (Eds.), Proceedings of 2nd International Kimberlite Conference, Washington D.C. AGU, pp. 129–139.

Tiller, W.A., 1991. The Science of Crystallization – Microscopic interfacial phenomena. Cambridge University Press, Cambridge.

Ulianov, A., Muntener, O., Ulmer, P., Pettke, T., 2007. Entrained Macrocryst Minerals as a Key to the Source Region of Olivine Nephelinites: Humberg, Kaiserstuhl, Germany. Journal of Petrology, 48, 1079-1118.

Ulmer, P., Sweeney, R.J., 2002. Generation and differentiation of group II kimberlites: Constraints from a high-pressure experimental study to 10 GPa. Geochimica et Cosmochimica Acta, 66, 2139-2153.

3. Kimberlite Ascent: Insights from Olivine[2]

3.1 Introduction

Olivine is volumetrically the most abundant phase in kimberlite deposits, and attends the ascent of kimberlite from source to eruption. As such, it 'experiences' the same physical and chemical changes that kimberlite melt/fluids do. Textural features within olivine record physical and chemical changes of the ascending magma, and therefore can be used to elucidate transport and eruption processes.

In this chapter textural features in kimberlitic olivine are document with the aim of constraining processes operative during kimberlite ascent and eruption. The samples used in this study derive from the Diavik Diamond Mine, N.W.T. They are the same sample set as described in chapter 2 with the exception that the pyroclastic rocks are omitted. Coherent kimberlite deposits at Diavik contain 40 – 50 volume % olivine, and have not been altered, as such; the mineralogy and most of the primary volcanic features are preserved. The groundmass mineralogy comprises monticellite, apatite and oxides (perovskite, spinel-ulvöspinel, chromite) and often are enclosed by carbonate or set in a mesostasis of carbonate and serpentine.

Several authors have documented that much of the olivine in kimberlite features distinct overgrowths (Kamenetsky et al., 2008; Carter Hearn, 2004; Brett et al., 2008). The recognition of overgrowths in olivine is, in part, a corollary of having fresh deposits that contain olivine has not been serpentinized. Textural information (overgrowths) is lost in deposits that have been subject to even minor serpentinization, and this alteration

[2] A version of this chapter is in preparation to be submitted for publication. Brett, R.C., Russell, J.K., (2009) Kimberlite Ascent: Insights from olivine. EPSL, 2009.

affects the majority of kimberlite deposits. The olivine at Diavik is well preserved and is not serpentinized. These olivines consist of two types based on shape and size; 1) medium to coarse-grained (< 2 cm), rounded to sub-rounded grains (olivine-I), and 2) fine-grained (< 1 mm), euhedral to subhedral crystals (olivine-II). In chapter 2 we showed that both populations are made up of a xenocrystic core and an overgrowth, implying that olivine in kimberlite is dominantly xenocrystic regardless of shape and size. The olivine-I population has thin overgrowths with respect to their cores, preserving the original shape of the grain, whereas olivine-II crystals have relatively thicker overgrowths that change the shape of the grains to euhedral. Many crystals are not zoned in the smaller euhedral population, and are phenocrystic in origin. The cores of all olivine are generally rounded in shape, and have smooth edges. Olivine crystallization on the rounded xenocrysts has trapped inclusions of melt, fluid and solid phases in the overgrowths, and in the phenocrysts. The rounded cores of both populations are ubiquitously fractured, and contain multiple populations of cracks, whereas the overgrowths and phenocrysts are fracture-free.

Below, these textural features are re-examined in detail, with the intent to establish their relative timing. These features are then related to specific geological processes with semi-quantitative calculations to extract the depth of formation of each feature, and thereby constrain processes operative during the ascent of kimberlite.

3.2 Textural features in olivine

The earliest features in the xenocrystic cores of kimberlitic olivine are multiple sets of cracks or fractures (Fig. 3.1). There are two modes of cracks in olivine, i) impact, and ii) tension cracks that are distinguished here by the orientation and material infilling

the fracture. Fractures that are produced from point collisions develop at a point and radiate outward from that point as semi-circular cracks (Swain & Atkinson, 1978). Tension cracks are produced by rapid decompression and generally occur in parallel along cleavage planes (Tingle, 1988; Hurai et al., 2008). In these rocks the tensional cracks comprise two textural varieties: sealed cracks and healed cracks.

When describing fluids that are have been trapped in crystallized olivine, and fluids trapped in fractures, the terms ‘primary inclusion’ and ‘secondary or pseudo-secondary inclusion’ are used respectively (c.f. Roedder, 1984). Primary inclusions are inclusions that have been trapped during growth of a mineral. Fluids derived from the melt that have invaded fractures are termed pseudo-secondary inclusions, and post-emplacement fluids trapped in cracks are termed secondary inclusions. Below, we describe sealed and healed fractures observed in xenocrystic olivine, and discuss the origin of the inclusions.

Figure 3.1. Photomicrographs, secondary electron (SE) and backscatter micrographs (BSE) of olivine from Diavik kimberlite deposit showing features of decompression cracks.
a) xenocrystic olivine (ol) showing sub-parallel, linear decompression cracks filled with carbonate (carb), b) high magnification of one of these carbonate-filled cracks, c) 3-dimensional image SE image of xenocryst broken along a crack plane showing a rough, continuous plan of carbonate, d) BSE image showing oxides trapped in sealed Sr-calcite (Sr-cc) crack, e) micrograph showing a healed fracture that overprints the sealed carbonate-filled fracture, f) enlarged view of pseudo-secondary inclusions in olivine showing textures commonly described as different stages of the healing process.

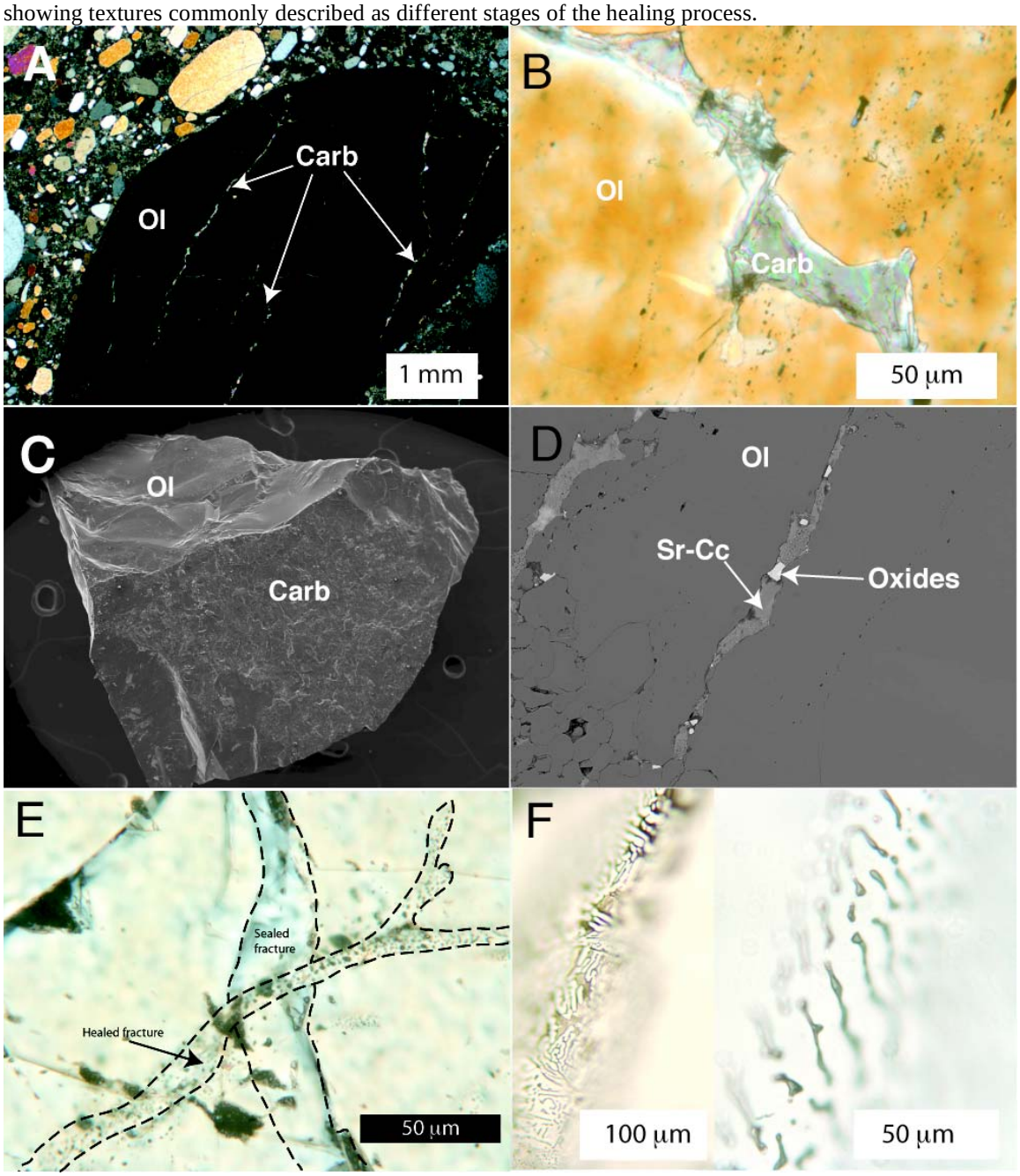

3.2.1 Sealed tension cracks

Sealed cracks occur when external fluids invade void space that was created by cracking, and cement the cracks shut. In these rocks this variety of fracture consists of tens of sub-parallel cracks of varying aperture (<5 μm) that are sealed with Sr-Ba enriched carbonate (Fig. 3.1 a-d). In cross-section, the carbonate in-fill can appear to be discontinuous, but define a linear trend marked by patches of elongate carbonate (Fig. 3.1a). Figure 3.1b is a higher magnification of the same sealed crack and shows that although fractures are planar-parallel, at a smaller scale the fracture surface is conchoidal. In order to examine these cracks in three-dimensions olivine grains were lightly 'tapped' until they broke apart along these pre-existing planes of weakness (Fig. 3.1c). The exposed fracture surfaces are continuous throughout the entire crystal. The continuity of these planes in three dimensions shows that the apparent discontinuous linear carbonate patches often observed in two-dimensions, may be an artifact of the small, irregular pathways formed when the crystal cracks. The carbonate-filled cracks also contain other solid phases (Fig. 3.1d). These phases are semi-quantitatively identified as Mg-chromite (cores) with spinel and spinel-ulvöspinel overgrowths (rims).

Sealed cracks do not extend to the crystal margins. Rather they terminate at the core-overgrowth interface (Fig 3.3c). This feature requires the formation of the cracks to pre-date the olivine saturation event, causing the overgrowths. In addition to the sealed cracks, there is abundant textural evidence that subsequent cracking events occur, and have been partially healed to fully healed.

3.2.2 Healed tension cracks

The formation of healed cracks is a more complicated process than the formation of sealed fractures. This process begins in a similar way to sealed cracks, in that external fluids in-fill void space created by cracking. Dissolution and crystallization of the host mineral along crack surfaces (i.e. olivine) decreases the surface energy, and drives the fluid to form spherical shapes surrounded by the newly crystallized host mineral (Roedder, 1984). A spectrum of inclusion morphology is observed of the sealed cracks, that range from inclusions that form planes of inclusions that are small and spherical. Intermediary textures range from, Swiss cheese-like patterns, to long tube like inclusions. The process of healing a fracture is termed necking-down (Roedder, 1984).

Healed cracks occur as a second generation of cracks, because they overprint the above described sealed cracks (Fig. 3.1e). These cracks are marked by a variety of spherical to elongated inclusions (Fig. 3.1f right), and networks of brownish, curvilinear, fluidal-like inclusions (3.1f left). Spherical inclusions are typically < 5 μm in diameter, have transparent centers and dark brown rims (Fig 3.1f). The elongate inclusions have a maximum width of 5 μm and can be 5 times as long. These inclusions are consistent with textures produced by necking down, and are indicative of healed fractures. At the time of formation, the surface area of the inclusions was probably much larger, and may have filled the cracks as continuous planar sheets (e.g. similar to the above described sealed cracks). Many healed fractures have carbonate inclusions that follow a linear trend in the xenocrystic core (Fig 3.3c). This figure shows an olivine grain with a forsterite rich core (see caption for false colour explanation). Olivine that has crystallized along this trend

has the same composition as the overgrowth, and surrounds the Sr-Ba rich calcite, trapping it as melt inclusions.

These healed cracks also occur as sub-parallel networks and are much more numerous than the sealed crack networks. The cracks extend throughout each crystal, and like the sealed cracks, terminate at the core-overgrowth interface (rather than at the crystal margin). The formation of these cracks is interpreted to be related to decompression of the crystal because the cracks are sub-parallel and they are bound by overgrowths. These features suggest that decompression occurred prior to crystallization because they are bounded by the overgrowths. Any material that was trapped in the cracks is primary material that is presently preserved (e.g. pseudosecondary inclusions; Roedder, 1984).

3.2.3 Rounding of macrocrysts

Xenocrystic olivine forms the cores to most olivine grains, regardless of size. The shapes of the xenocrystic cores are preserved by later overgrowths of olivine, and are typically rounded. Figure 3.2a is a secondary electron image that shows the 3-dimensional morphology of a typically well-rounded olivine macrocryst. Macrocrysts have an aspect ration of between 1:1 and 2:1 (Moss et al., 2008), and range from circular to oval in cross-sectional shape, and irregular ovoid shapes in 3-dimensions. The surfaces of rounded grains are characterized by stippled textures, and some striations (Fig 3.2b). Zoning patterns in olivine show that the cores of all types of olivine are rounded to sub-rounded in shape (e.g. Kamenetsky et al., 2008). Figure 3.2c shows a well-rounded, partially re-crystallized xenocryst rimmed by a thin overgrowth, and implies that the overgrowth happened after rounding occurred.

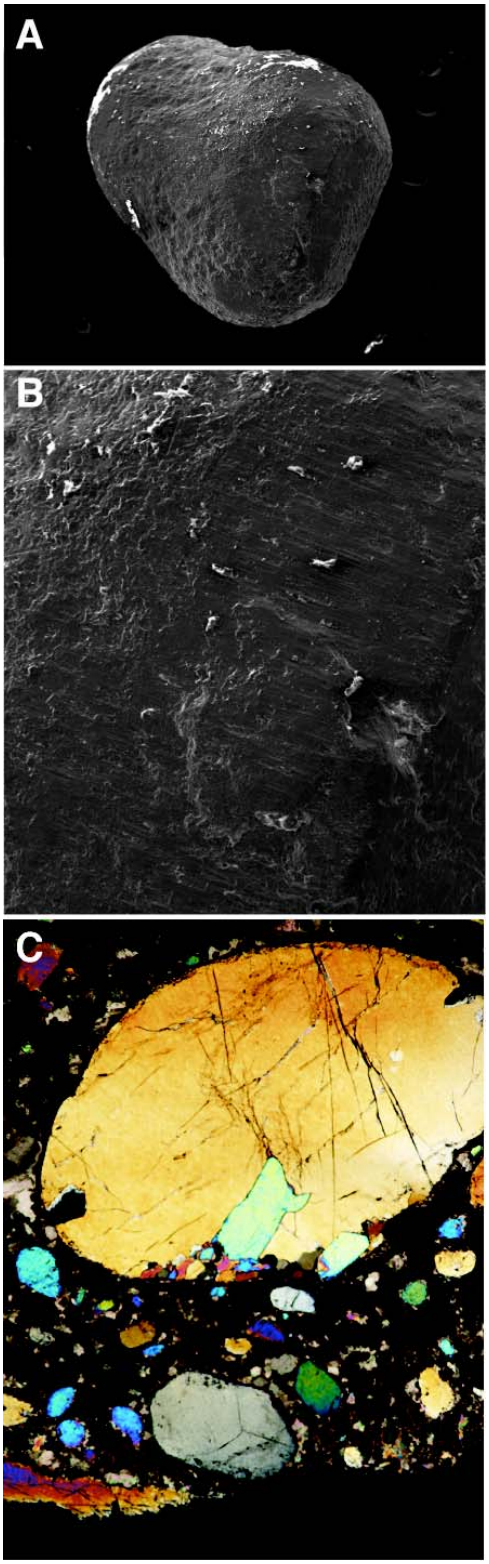

Figure 3.2. Secondary electron images and photomicrographs show rounded olivine xenocrysts.
a) 3-dimensional image of a rounded olivine xenocryst, b) the surface of this grain showing striations and pocked appearance. The grains are often smooth but not polished, and c) photomicrograph of a typical rounded olivine xenocryst with recrystallized textures and a thin overgrowth. The crystal has an aspect ratio of ~2:1 showing that crystals are often smooth but often are not perfectly spherical.

3.2.4 Olivine saturation and inclusions

The presence of overgrowths on all pre-existing olivine xenocrysts directly indicates that after decompression cracking and rounding of mantle olivine, the melt became saturated in olivine. Olivine saturation caused crystallization of olivine overgrowths on all xenocrystic olivine, and a volumetrically smaller fraction of olivine phenocrysts. Petrographically visible overgrowths are partly defined by the presence of mineral, fluid and melt inclusions. The interface of the core-overgrowth boundary is commonly marked by the presence of numerous, small (< 5 μm) spherical fluid inclusions that form 'bubble' planes marking the core-overgrowth boundary (Fig. 3.4a). Mineral inclusions are small at this boundary (< 1μm) but increase in size towards the edge of the crystal. Mineral inclusions are identified petrographically as opaque oxides, rutile and perovskite. There are larger (<60 μm), irregular-shaped inclusions in overgrowths which are dominantly composed of carbonate with other accessory solid phases (Fig. 3.4b and c), and are interpreted to be melt inclusions. There are several examples of precipitates on the polished surface of crystallized olivine (Fig. 3.4d). These precipitates may be caused by decrepitation of inclusions during thin sectioning, or form when under vacuum conditions during the carbon coating process (Kamenetsky, personal communication). Semi-quantitatively, the precipitates are composed of Na-K chlorides.

Primary inclusions trapped in overgrowths show a different morphology than the healed pseudo-secondary inclusions trapped by decompression cracks (Fig 3.3a). Inclusions in the overgrowth (o) are smaller (most are < 2 μm), spherical and outline the overgrowth, whereas inclusions in fractures in the core are larger, show necking features.

These types of inclusions and are only present as planar sections that cut the cores, but terminate at overgrowths (Fig 3.3a-b).

Figure 3.3. Photomicrographs and back-scattered images showing crack and overgrowth relationships.
a) healed crack in olivine (h) showing melt/fluid inclusions in olivine xenocryst, and fluid, melt and solid inclusions trapped in a thin overgrowth (o). The larger pseudo-secondary inclusions terminate at the overgrowth, where primary inclusions are much smaller and only are found at the perimeter of the crystal, b) decompression crack in an olivine xenocryst that terminates at the overgrowth boundary. This is evidence that cracks pre-date the overgrowths in relative timing, and c) false colour backscatter image of smaller, euhedral olivine-II crystal. Darker red is forsterite-rich, lighter red tones are less forsterite rich in composition and orange colours are carbonate. The dark red core is xenocrystic in origin, and the lighter red rim is an olivine overgrowth.

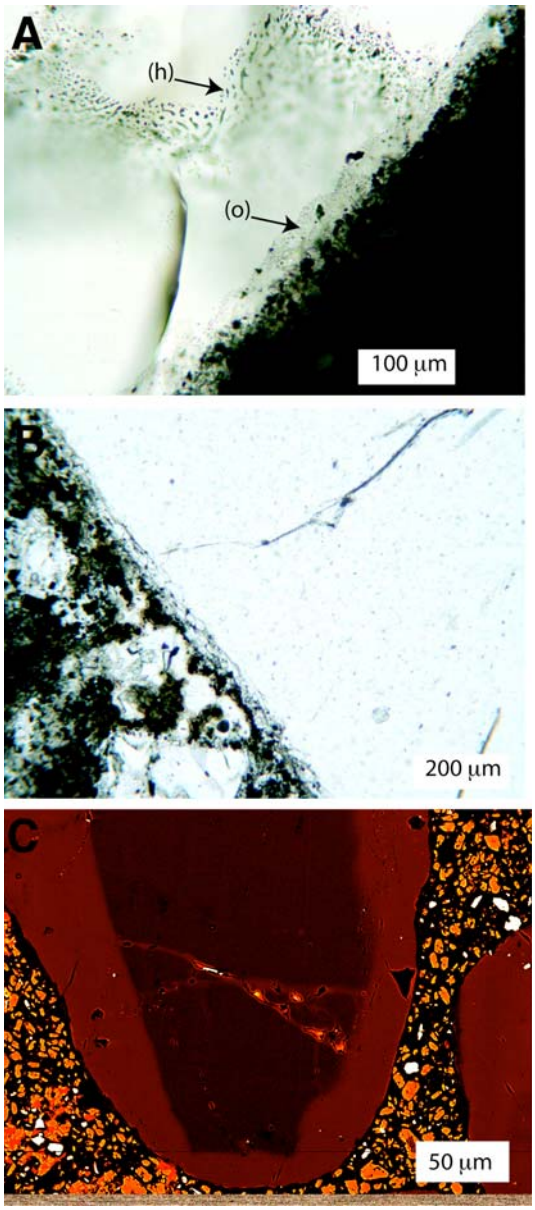

Figure 3.4. Photomicrographs and backscatter images of olivine showing inclusions trapped in overgrowths and phenocrysts.
a) olivine-II crystal showing planes of fluid inclusions and solid phases trapped in an overgrowth, b) olivine phenocryst with several irregular shaped carbonate melt inclusions, c) high magnification view of a carbonate melt inclusion (m) in an overgrowth, and d) decrepitated inclusion (due to decompression while under vacuum when carbon-coating) with precipitates are semi-quantitatively composed of Na and K chlorides.

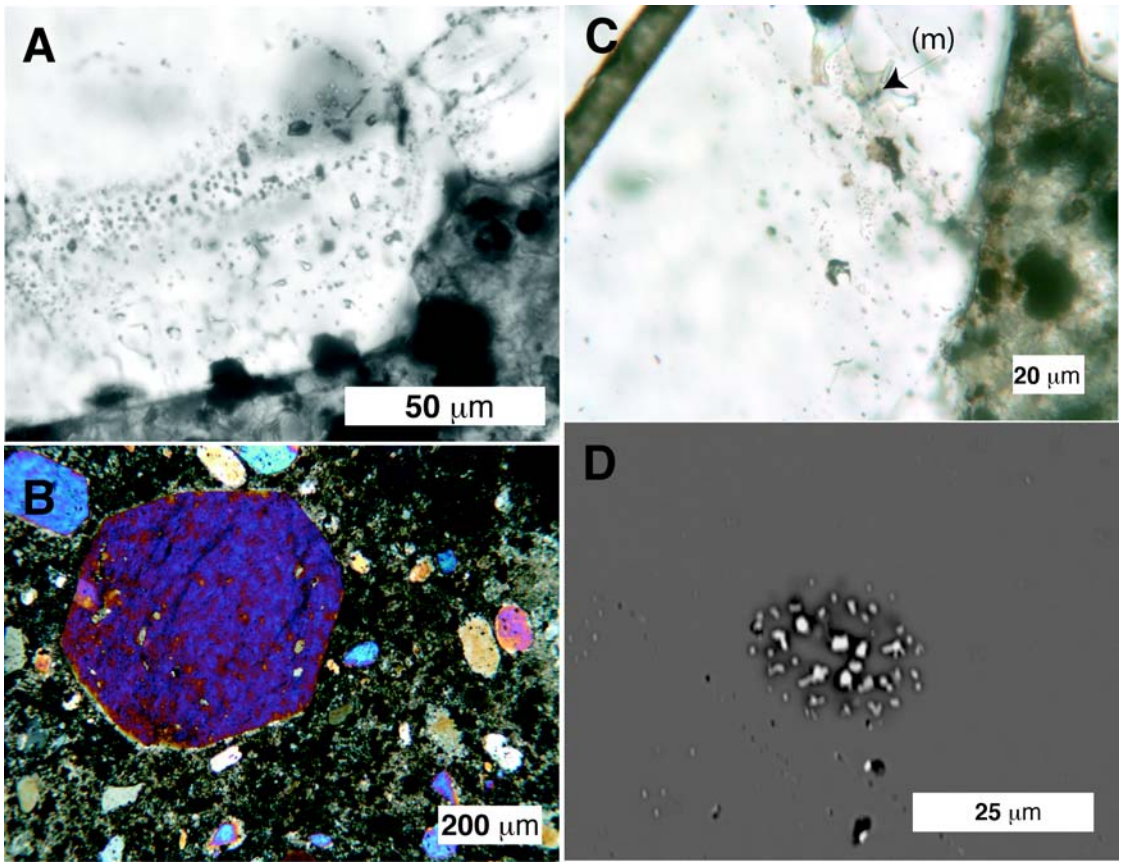

3.3 Textural record of ascent

The physical properties of olivine control the disaggregation of mantle xenoliths, tensile stress needed to crack crystals and crystal-fluid milling efficiency. Additionally, processes such as crystal cracking and olivine growth effectively trap melt, solid phases and fluids; these trapping events record important information on the chemical state of the system at the time of these events. The following analysis establishes a variety of constraints on kimberlite ascent. The textural features that elucidate kimberlite ascent processes include: tensional fractures, trapped phases in these fractures, rounded grains

and olivine overgrowths. In this section, the depths at which these features are produced are semi quantitatively constrained by calculations based on the physical properties of olivine.

3.3.1 Formation of fractures in olivine xenocrysts

This section presents the rationale for the creation of decompression cracks, with the intent of constraining the minimum distance at which crystals crack after being transported from their source. This is important because when crystals crack, chemical information is recorded by the identity of the phase that fill the void space. The parameters that ultimately control the brittle failure of olivine are: i) the pressure drop between the source (high P) and the pressure in the magma (lower P), and ii) the tensile strength of the crystal. The pressure drop is simply caused by the transportation of the magma and crystals to lower pressures. Crystals will resist this decompression until the yield strength of the crystal is reached, at which point the crystal will fail in tension. The tensile strength has been measured for olivine to vary between 200 and 800 MPa (Roedder, 1984; Johnson & Jenkins, 1991); it requires pressure drops of this magnitude to cause olivine to fail in tension, and is corresponds to ~7 to 27 km transport distance. This is true for olivine in all volcanic systems subjected to rapid ascent. However, below I quantitatively describe the ascent and tensile failure of olivine taking in account the rheology of olivine (volume expansion). This is important because viscous expansion of olivine acts as to minimize the pressure drop caused by ascent.

3.3.1.1 Extraction of elastic properties from thermo-chemical data

The analysis begins by plotting the isothermal (1300ºC) molar volume of forsterite as a function of pressure, calculated with the Theriak-Domino software (de Capitani, 1994), which uses the Berman (1992) database of thermodynamic values. The molar volume of forsterite increases from high to low pressure (Fig 3.5a). This line represents the molar volume of olivine as a function of pressure. An infinitesimal change in pressure corresponds to a change in the molar volume; this defines the bulk modulus (K) for olivine:

$$K = -V\left(\frac{\partial p}{\partial V}\right)_T \qquad 3.1$$

Since solid phases have relatively small variations of V, only very small errors are introduced by assuming a constant reference volume (Anderson & Crerar, 1993). The curve shown in figure 3.5a has a relatively constant slope, and allows us to treat the bulk modulus as a constant value (K ~ 1.4E10^{11} Pa). This value is consistent with experimental values for the bulk modulus of forsterite high pressure (e.g. K = 1.4075 E10^{11}±0.02 Pa; Zha et al., 1996).

3.3.1.2 Elastic expansion

To facilitate this discussion in terms of the rheology of olivine we must convert figure 3.5a from thermodynamic values (P and V_m) to equivalent rheologic terminology, stress (σ) and strain (ε). An equilibrated crystal in a fluid at depth is at lithostatic pressure, and has a molar volume. When a pressure drop occurs, olivine can elastically expand to achieve a new molar volume. The change in molar volume caused by uniform decompression, can be converted into volume strain:

$$\varepsilon = \frac{V - V_o}{V_o} \qquad 3.2$$

where V is the molar volume of olivine at the pressure of interest and V_o is the reference molar volume of olivine. The bulk modulus of olivine (calculated above) relates differential stress to this elastic volume strain (equation 3.3):

$$\sigma = K\varepsilon \qquad 3.3$$

Figure 3.5b is a plot of stress difference vs. volume strain. The x-axis represents the elastic change in volume of olivine in response to a change in stress. Olivine will expand as long as there is a stress difference between it and the surroundings. When a crystal expands, the stress difference between the crystal and its surroundings continually decreases to zero, at which point the crystal attains a new 'equilibrium' molar volume. The elastic expansion of olivine, however, does not account for the time scale of expansion, that is, how fast a crystal can release the stress (relax) in response to an imposed pressure drop.

3.3.1.3 Viscous relaxation

The principal mechanisms of compression (and therefore decompression) for minerals involve continuous changes in either bond angles and/or bond lengths (Lang, 2007). If the relaxation of olivine's structure is due to decompression, then viscous processes describe the rate of relaxation. Relaxation in many solids occurs over long time scales and can be treated as Newtonian (Poirier, 2000). The Newtonian viscosity of a material is defined as:

$$\eta = \frac{\sigma}{\dot{\varepsilon}} \qquad 3.4$$

,where σ is the deviatoric stress and $\dot{\varepsilon}$ is the strain rate. Strain rate is defined as,

$$\dot{\varepsilon} = \frac{d\varepsilon}{dt} \qquad 3.5$$

where $d\varepsilon$ is the change in volume strain and *dt* is the time interval. Times scales for volume relaxation have been shown to be identical to that measured for shear relaxation (Webb, 1997). The viscosity of 'dry' olivine at pressure has been measured to be approximately 10^{20} Pa. The viscosity, however, is reduced by orders of magnitude if saturated by OH (10^{17} Pa; Karato and Jung, 2003), and is a possible side effect of being in a kimberlite melt (Matveev & Stachel, 2007). For Newtonian materials, one can immediately plot the stress-strain rate curve for a phase if the viscosity is known (Fig. 3.5c). On figure 3.5c the range of tensile strengths for olivine (200 -800 MPa) is plotted as a grey band (c.f. Johnson & Jenkins, 1991). The stresses correspond to a strain rate at which tensile failure will occur (i.e. 2E-14 to 8E-14 s^{-1}). The magnitude of the pressure drop ultimately dictates the strain rate of the crystal. In order determine if the crystal has reached its critical strain rate (and hence fail), we must discuss the velocity of ascent in kimberlitic systems.

3.3.1.4 Transport velocity and crystal cracking

Decompression rates are proportional to the ascent rate (velocity) of kimberlite. Time vs. the stress difference is plotted for 3 different ascent paths (Fig. 3.6). The slope of each line is proportional to the ascent velocity (1 and 20 m/s). It is the purpose here to calculate the stress difference between the crystal and surroundings as a function of time. This requires knowledge of i) the strain rate of the crystal and ii) the pressure drop imposed on the crystal due to ascent; both quantities are dependent on time. I chose to

solve this problem numerically using incremental pressure drops to calculate the strain rate (stress release) and pressure drop (stress increase) as a function of time. In order to compute a solution, the pressure drop was incrementally increased until the stress difference exceeded the tensile strength of forsterite (i.e. 500 MPa) for each ascent velocity (See Appendix D for solution). Points of failure are marked by closed circles, and define a tensile strength curve as a function of time (hashed lines). This curve is linear, where the y-intercept is equal to the tensile strength of olivine and the slope is a function of the bulk modulus and viscosity of forsterite. The tensile strength a curve is plotted on figure 3.6 and represents the wet viscosity reported for olivine (wet; 10^{17}).

Figure 3.5. Thermodynamic, elastic and rheological relationships for forsterite.
a) molar volume vs. pressure curve for forsterite at 1300ºC, b) stress vs. volume strain curve for forsterite. The slope of this curve is the bulk modulus of forsterite, and c) strain-rate vs. stress curve for 'wet' forsterite (viscosity = 10^{17} Pa s). The grey solid line denotes a range of stress differences that would cause tensile failure of olivine. The arrows denote the corresponding strain rates at which failure occurs.

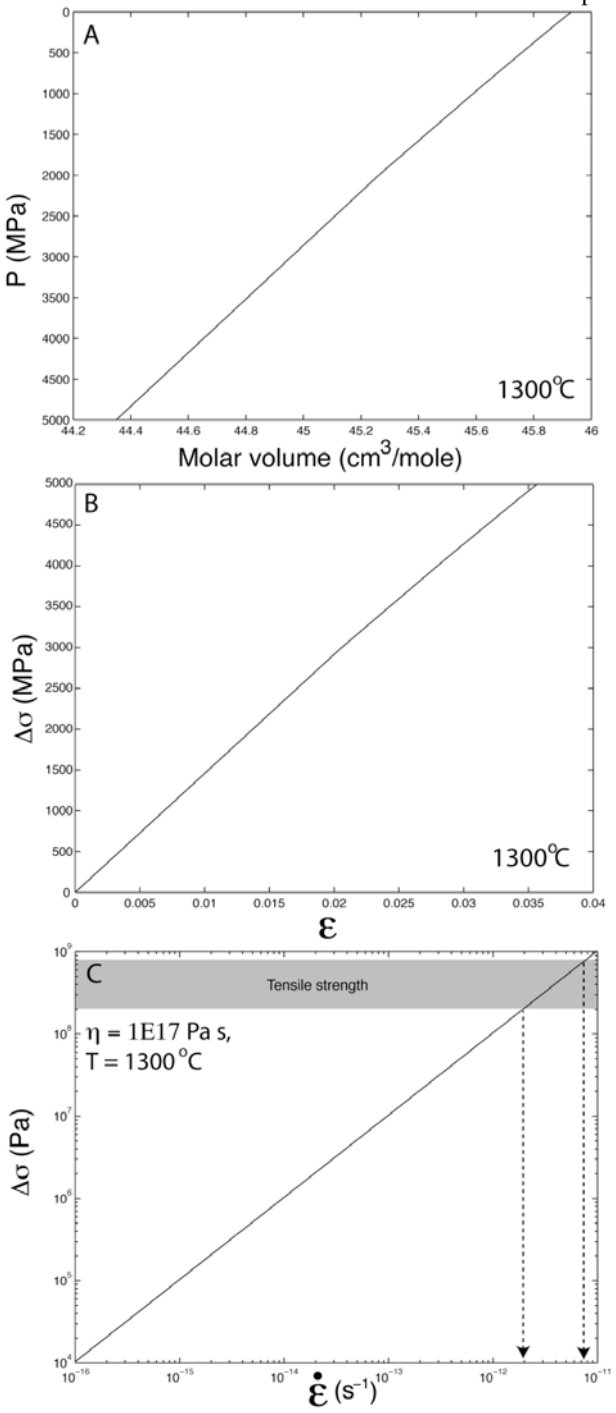

3.3.1.5 Results and discussion

For rapid ascent rates as reported for kimberlite (c.f. Sparks et al 2006; 1-20 m/s) very little stress is released due to viscous expansion during ascent, and for wet olivine the crystals crack ~16.6 km above their source, and travel for 14 to 4.7 hours. Crystals that source from great depths (i.e. ~200 km) will crack at comparable depths (~180 - 170 km), and will subsequently siphon and trap phases present at these depths. It is interesting that only rapid ascent rates can produce decompression cracks in 'wet' olivine. This is because the viscosity is low enough that the crystals can release the stresses caused by decompression at a faster rate. If the ascent of kimberlite were slower, crystals would relax viscously, and never reach their tensile strength.

In conclusion, at ascent rates thought to operate in kimberlite deposits, crystals crack approximately 17 km above their source. Although the crystals will continually crack from this point to the surface, we submit that the first cracking event releases the most energy, and thus produces the largest cracks. Subsequent cracking events are partially accommodated by releasing the energy along the initial crack surfaces as well as forming new, smaller cracks. This may explain the larger aperture sealed cracks that are overprinted by thin aperture healed cracks. Sealed cracks are filled with the melt/fluid that surrounds the crystal with some, previously crystallized oxides, and represents the most primitive kimberlite phases. As decompression continues, crystals continually crack to release the constant increase in stress during ascent. These later cracking events are possibly less energetic because some of the energy is dissipated on the pre-existing planes of sealed cracks. These smaller healed cracks happen later in ascent than the sealed cracks but also siphons fluid. These types of cracks may be more amendable to

healing because of the smaller crack aperture, and in some examples (Fig. 3.3c) occur concurrently with olivine saturation.

Crystal cracking may also aid in the disaggregation of mantle xenoliths. Crystals within xenoliths, crack due to decompression from transport. Slight volume changes occur for each crack that is produced. The summation of all of the crystals slight increases in volume causes compressional stresses along grain boundaries, and may facilitate the efficient disaggregation of xenoliths that are observed in kimberlite (i.e. xenocrystic-rich deposits).

Figure 3.6. Model for the formation of decompression cracks in forsterite.
Time vs. pressure diagram showing tensile failure envelop (dotted line) for a range of ascent rates (shaded region). The tensile strength curve is plotted for viscosities corresponding to wet olivine. The intersection of these curves with the ascent velocity curves defines the depth at which tensile failure occurs from source, and defines an ascent distance.

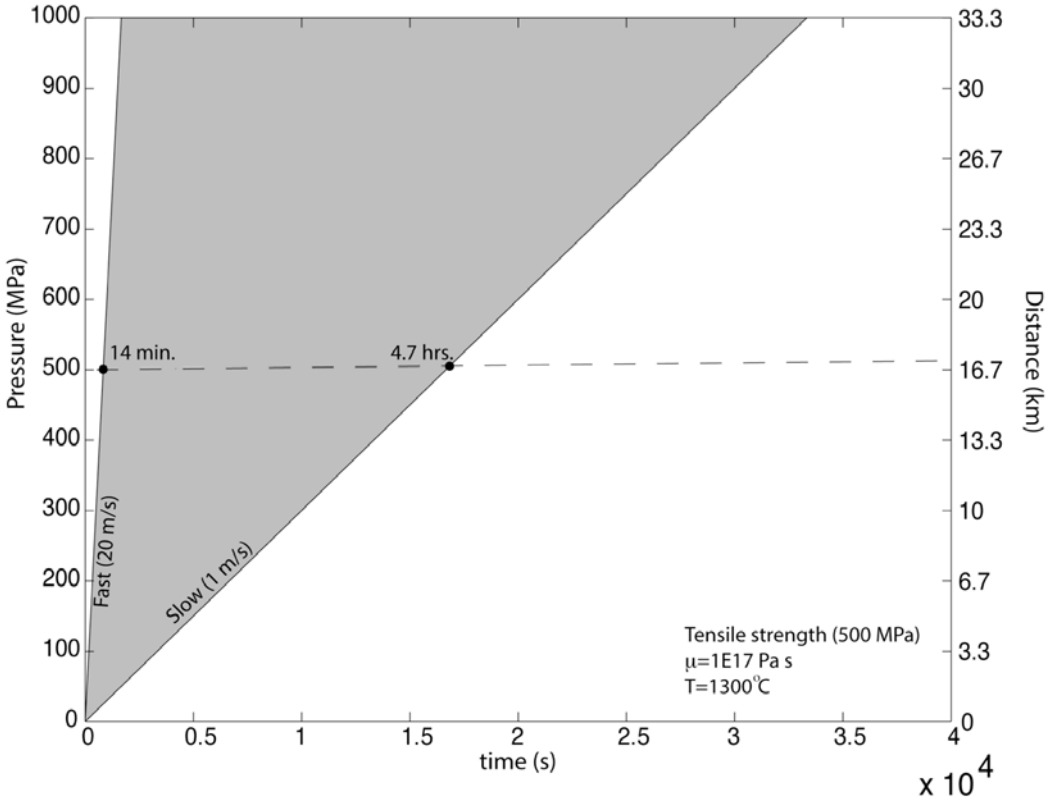

3.3.2 Trapping of inclusions in cracks

The change in volume created by a decompressed crystal results in small planes of open pore space that are by definition under near vacuum conditions. We interpret that phases presently observed in olivine cracks have resulted from decompression cracking that subsequently siphons and samples phases external to the crystal. The space produced by cracking can be filled by solid, liquid and supercritical phases if the crack breaches the edge of the crystal. For example, if olivine sources from great depths (200 km), then decompression cracking occurs at comparable depths (180 km), and will siphon off fluid and crystals into these cracks. The presence of carbonate and oxides in these cracks is evidence that, i) oxide phases have crystallized at great depth, and ii) the kimberlite melt/fluid crystallizes carbonate that is high in Sr and Br (c.f. Armstrong et al., 2004).

The composition of carbonate in the decompression cracks is > 90% $CaCO_3$, and implies that the kimberlite melt became saturated in calcite. Experiments on $CaCO_3$-$MgCO_3$ solid solutions show that at high pressure (1 GPa) calcite is the only stable carbonate phase if the melt is composed of < 20 mole% of the $MgCO_3$ component. For carbonate melt compositions that have > 20% $MgCO_3$ dolomite + calcite is the stable carbonate assemblage (Buob et al., 2006). Experiments on partially melted carbonated peridotite produce melt with Ca/(Ca + Mg) of 0.41 (Dasgupta and Hirschmann, 2007), and requires dolomite stability from a fluid derived from the partial melting of carbonated peridotite. Furthermore, experiments done on carbonate-bearing peridotite in the CaO-MgO-SiO_2-CO_2 system shows dolomite to be the stable carbonate phase at pressure, but to break down rapidly during decompression to produce a CO_2 fluid (Canil, 1990). It is unlikely that melt would crystallize pure calcite. Instead, the fluid that has crystallized

this carbonate may have precipitated from an evolved primary kimberlite melt or fluid at high pressures.

3.3.3 Rounding

Rounding of crystals in an igneous context can happen by means of chemical dissolution (Boudier 1991, Rosso & Rimstidt 2000, Chen & Brantley 2000, Donaldson 1985) or mechanical abrasion (Afanas'ev et al. 2008). The boundary between cores and the overgrowths within the Diavik deposits are predominantly sharp with respect to forsterite zoning (e.g. Fig. 2.3a), however a minor population is observed to have a gradational Mg-Fe boundary, showing embayed features reminiscent of dissolution (e.g. Fig. 2.3c). It is probable that olivine had become unstable with respect to the kimberlite melt at some point before becoming saturated, and produces textures as seen in Fig. 2.3c. Dissolution of olivine cannot be the limiting factor in terms of shape modification because the cores are dominantly very rounded as shown incontrovertibly in olivine-I grains (Fig. 3.2c, 3.3b, 2.1c) and have sharp boundaries. The surfaces of olivine xenocrysts in kimberlite are relatively smooth (see Fig. 3.2c), but show some roughness observed as stippled and striated features. Evidence of resorption seen as embayments or other corroded features is not observed to be a ubiquitous texture in olivine xenocrysts. This is supported by a thermodynamic analysis that concludes olivine to be the most stable mantle mineral in kimberlite magmas (Luth, 2008). For these reasons mechanical shape modification caused by smaller abrasive particles change the shapes to anhedral or rounded shapes, and is assumed the dominant rounding mechanism. Efficient rounding by mechanical means requires a fully turbulent fluidized system. It is impossible to constrain at what depth rounding occurs, it is possible that mechanical rounding occurs to

have rounding occur from source to eruption if kimberlite ascent is fluidized and turbulent. However it is also possible that punctuated, violent bursts of ascent to round a crystal very quickly on relatively short distances. Regardless, continuous ascent and punctuated ascent models of kimberlite can mill, and round particles, probably for most of the ascent.

Figure 3.7. Schematic model of olivine transport
Cartoon that illustrates the sequence of events that operate on olivine to produce the observed textural features. The sequence begins at the bottom of the column at 200 km, but could extent to greater source depths. Arrows indicate the depth at which each feature is constrained to. Dotted lines followed by question marks indicate uncertainty on the on where the feature stops or starts.

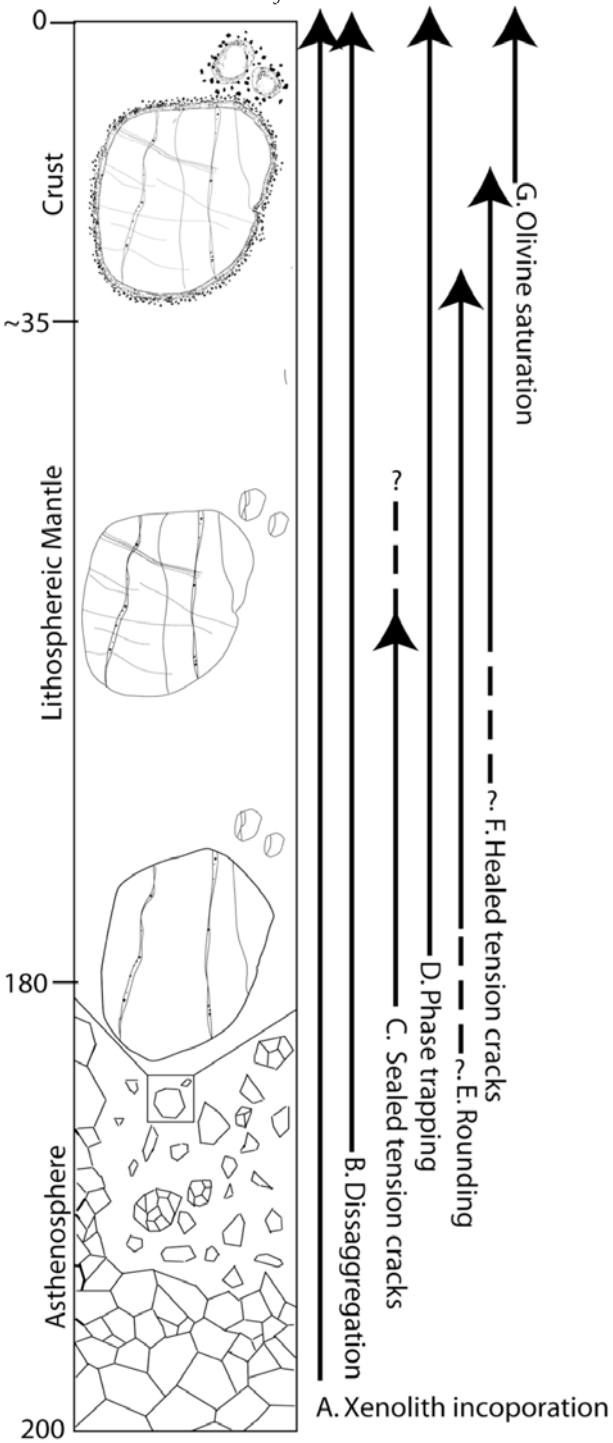

3.3.4 Saturation depth

The saturation of olivine in kimberlite magmas causes growth of olivine, which traps phases (solid, liquid and/or gas), preserving them as intracrystalline inclusions. Effervescence of volatile phases (i.e. CO_2) is facilitated by nucleation on preexisting xenocrystic surfaces (Roedder, 1984). Contemporaneous saturation and growth of olivine traps these bubbles as planes of fluid phases inside the crystal (see Fig. 3.3a and 3.4a). Minerals that contain fluid and melt inclusions experience dilatational stress during eruptions. Dissolved volatile components in the inclusions have a bulk modulus much less than that of the crystal (Tait, 1992), and only limited amounts of decompression can take place until the crystal fails in tension. Stresses in the host crystal decrease rapidly at a similar scale to the inclusions radius (Tait, 1992). The inclusions observed in olivine overgrowths however, do not seem to have decrepitated. This implies that the overgrowths have not passed through the critical pressure drop needed to cause tensile failure of the crystal. This is advantageous because we can use this fact to estimate a minimum crystallization depth.

The tensile strength of olivine has been experimentally estimated using synthetic and natural olivine by recording the pressures changes required to decrepitate fluid inclusions (Johnson and Jenkins, 1991; Roedder, 1984). The results of these studies indicate that decrepitation is dependent on the size of the fluid inclusion; smaller inclusions require larger pressure differences to decrepitate than do larger inclusions. The pressure drop needed to cause decrepitation of the fluid inclusions in these studies range from > 500 MPa in smaller inclusions (> 10 μm diameter) to ~200 MPa in larger inclusions. Fluid inclusions that did not decrepitate were therefore trapped at depths of 7

to 20 km maximum. Although a rough estimate, it is very important because this implies that olivine saturation must occur in the crust, and that all events that happened prior to saturation (rounding, tension cracking, vesiculation) have to occur at greater depths. This claim is supported by the fact that olivine phenocrysts do not suffer from the pervasive tension cracking as observed in xenocrysts.

3.4 Summary model

Olivine is incorporated into kimberlitic melts at great as peridotitic mantle xenoliths (Fig. 3.7a). Shortly after the incorporation of these xenoliths the tensile strength of the olivine is reached at a minimum of 20 km of ascent (Fig. 3.7c). Disaggregation (Fig. 3.7b) of mantle xenoliths is facilitated by expansion of the minerals comprising the xenoliths. The void space produced by the brittle failure of olivine is filled with melt and crystals consisting of primitive carbonate melt (i.e. high-Sr), chromite and spinel crystals (3.7d). The carbonate melt later crystallizes to produce sealed fractures (Fig. 3.7c). Cracking continues during ascent, however the latter cracks are smaller than the initial sealed, and are preserved as healed cracks (Fig. 3.7f). The mechanical rounding of the xenocrysts post-date, or occur contemporaneously with cracking events (Fig. 3.7e). Saturation of olivine causes rounded overgrowths on large xenocrysts, euhedral overgrowths on smaller xenocrysts, and a volumetrically minor population of olivine phenocrysts (Fig. 3.6g). Olivine growth traps fluid, solid and melt inclusions. The saturation of olivine in kimberlite melt occurs at a maximum depth of 20 km and a minimum depth of 7 km.

3.5 List of references

Afanas'ev, V. P., Nikolenko, E. I., Tychkov, N. S., Titov, A. T., Tolstov, A. V., Kornilova, V. P., Sobolev N. V. (2008) Mechanical abrasion of kimberlite indicator minerals: experimental investigations. Russian Geology and Geophysics, 49 91-97.

Anderson, G.M., Crerar, D.A. (1993) Thermodynamics in Geochemistry. Oxford University Press, p. 173.

Armstrong, J.P., Wilson, M., Barnett, R.L., Nowicki, T., Kjarsgaard, B.A., 2004. Mineralogy of primary carbonate-bearing hypabyssal kimberlite, Lac de Gras, Slave Province, N.W.T. Lithos, 76, 415-433.

Berman R.G. (1988) Internally-consistent thermodynamic data for minerals in the system Na_2O-K_2O-CaO-MgO-FeO-Fe_2O_3-Al_2O_3-SiO_2-TiO_2-H_2O-CO_2. *Journal of Petrology* **29** 445-522

Boudier, F., 1991. Olivine xenocrysts in picritic magmas: An experimental and microstructural study. Contributions to Mineralogy and Petrology, 109, 114-123.

Brett, R.C., Russell, J.K., Moss, S., 2008. The origin of olivine in kimberlite: Phenocryst or impostor. 9th International Kimberlite Conference Extended Abstract, No. 9IKC-A-00298.

Buob, A., Luth, R.W., Schmidt, M.W., Ulmer, P., (2006). Experiments on CaCO3-MgCO3 solid solutions at high pressure and temperature. American Mineralogist, 92, 435-440.

Canil, D., 1990. Experimental study bearing on the absence of carbonate in mantle-derived xenoliths. Geology, 18, 1011-1013.

Carter Hearn Jr., B., 2004. The Homestead kimberlite, central Montana, USA: mineralogy, xenocrysts, and upper-mantle xenoliths. Lithos, 77, 473-491.

Chen, Y., Brantley, S.L., 2000. Dissolution of forsteritic olivine at 65° and 2 < pH < 5. Chemical Geology, 165, 267-281.

Dasgupta, R., Hirschmann, M.M., (2007). A modified iterative sandwich method for determination of near-solidus partial melt compositions. II. Application to determination of near-solidus melt compositions of carbonated peridotite. Contributions to Mineralogy and Petrology, 154, 647-661.

de Capitani C. (1994): Gleichgewichts-Phasendiagramme: Theorie und Software. Beihefte zum European Journal of Mineralogy, 72. Jahrestagung der Deutschen Mineralogischen Gesellschaft, 6,48.

Donaldson, C.H. (1985) A comment on crystal shapes resulting from dissolution in magmas. Mineralogical Magazine, 49, 129-132.

Johnson, E.L., Jenkins, D.M. (1991) Synthetic H,O-CO, fluid inclusions in spontaneously nucleated forsterite, enstatite, and diopside hosts: The method and applications. Geochimica et Cosmochimica Acta, 55, 1031-1040.

Hurai, V., Prochaska, W., Lexa, O., Schulmann, K., Thomas, R., Ivan, P. (2008) High-density nitrogen inclusions in barite from a giant siderite vein: implications for Alpine evolution of the Variscan basement, Western carpthians, Slovakia. Journal of Metamorphic Geology, 26, 487-498.

Kamenetsky, V.S., Kamenetsky, M.B., Sobolev, A.V., Golovin A.V., Demouchy, S., Faure, K., Sharygin V.V., Kuzmin, D.V., 2008. Olivine in the Udachnaya-East Kimberlite (Yakutia, Russia): Types, compositions and origins. Journal of Petrology, 49, 823-839.

Karato, S., Jung, H. (2003) Effects of pressure on high-temperature dislocation creep in olivine. Philosophical Magazine, 83:3, 401-414.

Lange, R.A., 2007. The density and compressibility of $KAlSi_3O_8$ liquid to 6.5 GPa. American Mineralogist, 92, 114-123.

Luth, R.W., 2007. The activity of silica in kimberlites, revisited

Matveev, S., Stachel, T., 2007. FTIR spectroscopy of OH in olivine: A new tool in kimberlite exploration. Geochemica et Cosmochimica Acta, 71, 5528-5543.

Moss, S., Russell, J.K., Brett, R.C., Anderews, G.D.M., 2008. Spatial and temporal evolution of kimberlite magma at A154N, Diavik, Northwest Territories, Canada. Lithos, (submitted, 2008).

Poirier, J.P., 2001. Earth's Interior, 2nd Edition. Cambridge University Press.

Roedder, E., 1965. Liquid CO_2 inclusions in olivine-bearing nodules and phenocrysts form basalts. The American Mineralogist, 50, 1746-1782.

Roedder, E. 1984. Fluid Inclusions; Reviews in Mineralogy In Mineralogical Society of America.

Rosso, J.J., Rimstidt, J.D., 2000. A high resolution study of forsterite dissolution rates. Geochimica et Cosmochimica acta, 64, 797-811.

Sparks, R.S.J., Baker, L., Brown, R.J., Field, M., Schumacher, J., Stripp, G., Walters, A., 2006. Dynamical constraints on kimberlite volcanism. Journal of Volcanology and Geothermal Research, 155, 18-48.

Swain, M.V., Atkinson, B.K., 1978. Fracture surface energy of olivine. Pure and Applied Geophysics, 116, 866-872.

Tait, S., 1992. Selective preservation of melt inclusions in igneous phenocrysts. American Mineralogist, 77, 146-155.

Tingle, T.N., 1988. Retrieval of uncracked single crystals from high pressure in piston-cylinder apparatus. American Mineralogist, 73, 1195-1197.

Webb, S.L., 1997. Silicate Melts. Lecture notes in Earth Science, Springer.

Zha, C., Duffy, T., Downs, R., Mao, H., Hemley, R. J., 1996. Sound velocity and elasticity of single-crystal forsterite to 16 GPa. Journal of Geophysical Research, 101, 17535-17545.

4. Conclusions and further questions

This thesis describes several textures in kimberlitic olivine and arranged these textures in a chronological order. The main part of this work elucidated the origins of olivine in kimberlite using petrographic descriptions and geo-chemical statistics. The findings are that heterogeneous crystallization produces overgrowths on all pre-existing olivine xenocrysts and a volumetrically small fraction of homogeneous crystallization, and implies a smaller amount of crystallization than previously documented (5 vol. %). The reduced estimate of olivine crystallization has consequences to the primitive melt composition by lowering the Mg# of the melt, and to the dissolution of orthopyroxene. Growth models are constrained by observations of maximum overgrowth thickness and maximum phenocryst size. To more rigorously test these models a SEM map of an entire section be studied. To do this one would have to identify all of the zoned crystals and measure the diameter and overgrowth thickness. A large number of these measurements would allow us to use a particular growth model with confidence.

Secondary to this study, a series of textural features found in kimberlitic olivine have been described. In chronological order these features include: decompression cracks (sealed), decompression cracks (healed), rounding and olivine saturation. Using physical properties of olivine the depths that these textural features are produced are constrained. Consequently, phases are trapped in decompression cracks and in crystallized olivine, and consist of melt, fluid and solid inclusions. Although semi-quantitatively recognized that carbonate has more Sr at depth, a detailed chemical study on the inclusions was not completed. This would include: quantification of composition of the fluid (e.g. CO_2 or H_2O-rich), quantitative analysis of carbonate in sealed fractures, healed fractures, melt

inclusions, groundmass, and segregations (c.f. Roedder, 1984) . This would give a chemical evolution of carbonate in kimberlite from mantle to deposit. The textures produced by rounding may be masked by the overgrowths. To quantify rounding it maybe advantageous to look at other mantle derived minerals that have been rounded, but have not been overgrown (e.g. garnet, diamond), or perhaps attempt to reproduce rounding in a fluidized environment using analogue experiments. In addition, decompression experiments on single crystals would be beneficial as there is a paucity of studies on viscous relaxation of crystals. These experiments would add to an understanding of mineral physics in general, and may aid in resolving the rheological issue of where decompression cracks originate.

4.1 List of references

Roedder, E. 1984. Fluid Inclusions; Reviews in Mineralogy In Mineralogical Society of America.

APPENDIX A: Whole rock chemical compositions of coherent kimberlite

Table A1. Major (wt %) and trace element (ppm) whole rock chemical compositions of coherent kimberlite. Whole rock major oxide analyses were done by X ray fluorescence following a lithium metaborate fusion at Chemex Labs in North Vancouver, British Columbia.

Sample No.	1	2	3	4	5
SiO_2	33.28	29.62	30.39	29.92	26.66
TiO_2	0.88	1.10	0.75	0.85	1.27
Al_2O_3	1.70	1.53	1.29	1.48	1.68
Cr_2O_3	0.31	0.38	0.31	0.31	0.35
FeO(T)	7.91	7.61	7.57	7.47	7.77
MnO	0.16	0.16	0.16	0.16	0.19
MgO	38.75	34.50	38.51	37.52	36.80
CaO	7.46	9.90	8.83	8.23	11.54
Na_2O	b.d.l.	0.05	b.d.l	0.02	0.03
K_2O	0.30	0.36	0.03	0.08	0.05
P_2O_5	0.32	0.44	0.39	0.43	0.64
H_2O	1.77	2.61	3.70	3.46	4.65
S	0.06	0.08	0.07	0.07	0.09
CO_2	5.75	8.83	4.76	7.47	6.12
Total	98.65	97.17	96.76	97.47	97.84
LOI	7.58	11.40	8.90	11.30	11.60
CO_2/H_2O	3.25	3.38	1.29	2.16	1.32

APPENDIX B: Major and minor element compositions of olivine

(See attached CD)

APPENDIX C: Statistical analysis of olivine mineral chemistry

Below we describe the methods used to provide a statistical analysis of the chemical variations within and between olivine grains. The concentrations of each element or component were binned and plotted on a standard histogram. We used Lilliefors' composite goodness-of-fit test provided in Matlab Statistics toolbox to evaluate each of our data sets for normality. The Lilliefors' tests the null hypothesis that the data set is normally distributed with an unspecified mean and standard deviation at a 5% significance level. The alternative hypothesis is that the data set is not normally distributed. The test is a 2-sided goodness-of-fit test appropriate for situations where a fully specified null distribution is unknown.

Gaussian distributions are advantageous in that standard statistical methods can be applied to compare data sets and provide a quantitative method for describing genetic differences between populations. A two-sample T-test was used to test the hypothesis that two independent data sets come from distributions with equal means at the 5% significance level. The data are assumed to come from normal distributions with unknown, but equal, variances. Each bar in a graph has a width that corresponds to a range of composition. Distributions are shown as histograms where height of bar is proportional to the number of data (n) within the interval.

Each bar height is the probability the composition value is within the interval of the width of the bar centered on the mean value. The area under the histogram is the sum of the width of each bin multiplied by the height of each bar. To compare to the Gaussian distribution that has an area of 1, the histogram values were multiplied by the inverse of

the area under the histogram. Therefore all of the above bar graphs in Fig. 2.4 have an area of 1.

Table A2. Results of Student's t-Test for equality of means between samples for each group. Boxes marked with Fo and/or Ni mark instances where the null hypothesis is rejected.

Samples:	1	2	3	4	5
1			**olivine-I cores**		
2	--				
3	--	--			
4	--	--	--		
5	--	--	--	--	

Samples:	1	2	3	4	5	6	7
1					**olivine-II cores**		
2	--						
3	Fo	Fo					
4	--	--	--				
5	--	--	Fo	--			
6	--	--	Fo	--	--		
7	--	--	--	--	--	--	

Samples:	1	2	3	4	5
1			**olivine-I rims**		
2	--				
3	--	Ni			
4	--	--	Ni		
5	--	Ni	--	Ni	

Samples:	1	2	3	4	5	6	7
1					**olivine-II rims**		
2	--						
3	--	--					
4	--	Ni	--				
5	--	--	--	--			
6	Ni	Ni	--	--	--		
7	--	--	Fo	--	--	Fo/Ni	

Table A3. Results of students t-Test for olivine-I & II cores and rims tested for equal means in terms of NiO content.

	Ol-I core	Olivine-I rim	Ol-II core	Ol-II rim
Ol-I core				
Olivine-I rim	Ni			
Ol-II core	-	Ni		
Ol-II rim	Ni	-	Ni	

APPENDIX D: Model for the tensile failure of olivine

```
% Program to calculate pressure drop needed to cause Tensile failure
% cb_PvT_08.m
% Numerical solution to calculate the pressure drop needed to cause tensile
% failure of forsterite. Input parameters include: ascent velocity (v), the
% density of the overlying rock column, the viscosity of olivine (eta),
% the Bulk modulus of olivine (K), and tensile strength of olivine.

% Curtis Brett
% UBC, 2008

clear all
format long
% Variables to initialize and constants
v = 0.0001;     % ascent rate (m/s)
rhog = 30000;   % density * g (Kg m-1 m s-2)
eta = 1E20;     % viscosity of olivine (Pa s)
p_app = 0;      % Initial pressure difference between olivine & system (Pa)
K = 1.4E11;       % Bulk modulus (Pa)
mp = 10000000000;     % Max pressure
inc = 1000;     % Increment
t2 = 0;
TS = 500E6;        % Tensile strength of olivine
for i = 1:inc:mp
   dp      = inc + p_app;      % p inc (i) + the p 'felt' by crystal
   Ed      = dp/eta ;          % strain rate
   t       = i  / (v*rhog);    % time increment
   e_r     = Ed * (t - t2);    % amount of strain given Ed and t inc
   p_app = dp - (e_r*K);       % Pressure released
   t2 = t;                     % save time
   if p_app >= TS           % Break when p_app reaches tensile strength
      disp('Tensile strength reached')
      break
   end
end
% Output
disp(['Depth = ' num2str(v*t/1000) '(km)'])
disp(['Apparent depth = ' num2str(p_app/rhog/1000) '(km)'])
disp(['dp = ' num2str(rhog*v*t/1000000) ' (MPa)']);
disp(['Crystal feels = ' num2str(p_app/1000000) ' (MPa)']);
```

APPENDIX E: Measurements of olivine growth thickness

Figure A1. Measurements of mean diameter (mm), and growth thicknesses for 95 olivine grains. Measurements are made on a BSE map of a full thin section of coherent kimberlite associated with the A154N pipe, Diavik. The measured growth thickness is an apparent thickness because each grain is randomly cut at angles that are not orthogonal to the overgrowth surface. Apparent thicknesses are always larger than the true thickness of the overgrowth. These data show the apparent growth thickness is positively correlated with the observed mean diameter of the grain. Growth model C, surface area controlled growth, is the only model permissive with these data.